PCCP

ROYAL SOCIETY OF CHEMISTRY

PAPER

View Article Online
View Journal | View Issue

Check for updates

Cite this: *Phys. Chem. Chem. Phys.*, 2020, **22**, 368

Published on 20 November 2019. Downloaded on 12/31/2019 8:06:50 PM.

Structural and reorientational dynamics of tetrahydroborate (BH_4^-) and tetrahydrofuran (THF) in a $Mg(BH_4)_2$·3THF adduct: neutron-scattering characterization†

Mirjana Dimitrievska, *[ab] Marina Chong,[c] Mark E. Bowden,[c] Hui Wu,[b] Wei Zhou,[b] Iffat Nayyar,[c] Bojana Ginovska,[c] Thomas Gennett,[a] Tom Autrey,[c] Craig M. Jensen[d] and Terrence J. Udovic[b]

Received 11th June 2019,
Accepted 20th November 2019

DOI: 10.1039/c9cp03311d

rsc.li/pccp

Metal borohydrides are considered promising materials for hydrogen storage applications due to their high volumetric and gravimetric hydrogen density. Recently, different Lewis bases have been complexed with $Mg(BH_4)_2$ in efforts to improve hydrogenation/dehydrogenation properties. Notably, $Mg(BH_4)_2$·*x*THF adducts involving tetrahydrofuran (THF; C_4H_8O) have proven to be especially interesting. This work focuses on exploring the physicochemical properties of the THF-rich $Mg(BH_4)_2$·3THF adduct using neutron-scattering methods and molecular DFT calculations. Structural analysis, based on neutron diffraction measurements of $Mg(^{11}BH_4)_2$·3TDF (D – deuterium), has confirmed a lowering of the symmetry upon cooling, from monoclinic *C*2/*c* to $P\bar{1}$ *via* a triclinic distortion. Vibrational properties are strongly influenced by the THF environment, showing a splitting in spectral features as a result of changes in the bond lengths, force constants, and lowering of the overall symmetry. Interestingly, the orientational mobilities of the BH_4^- anions obtained from quasielastic neutron scattering (QENS) are not particularly sensitive to the presence of THF and compare well with the mobilities of BH_4^- anions in unsolvated $Mg(BH_4)_2$. The QENS data point to uniaxial 180° jump reorientations of the BH_4^- anions around a preferred C_2 anion symmetry axis. The THF rings are also found to be orientationally mobile, undergoing 180° reorientational jumps around their C_2 molecular symmetry axis with jump frequencies about an order of magnitude lower than those for the BH_4^- anions. In contrast, no dynamical behavior of the THF rings is observed with QENS for a more THF-deficient $2Mg(BH_4)_2$·THF adduct. This lack of comparable THF mobility may reflect a stronger Mg^{2+}–THF bonding interaction for lower THF/$Mg(BH_4)_2$ stoichiometric ratios, which is consistent with DFT calculations showing a decrease in the binding energy with each additional THF ring in the adduct. Based on the combined experimental and computational results, we propose that combining THF and $Mg(BH_4)_2$ is beneficial to (i) preventing weakly bound THF from coming free from the Mg^{2+} cation and reducing the concentration of any unwanted impurity in the hydrogen and (ii) disrupting the stability of the crystalline phase, leading to a lower melting point and enhanced kinetics for any potential hydrogen storage applications.

Introduction

Using hydrogen as an energy carrier provides an opportunity to achieve zero-emission propulsion, which will help to reduce the consumption of fossil fuels and limit the extent of anthropogenic contributions to climate change.[1] Storing hydrogen in chemical bonds, *i.e.*, hydrogen storage materials, is one approach to storing and transporting hydrogen that provides greater volumetric and gravimetric hydrogen densities compared to compressed hydrogen gas. Hydrogen storage materials must fulfill a wide range of requirements to be industrially applicable. Among these, a high hydrogen content, fast kinetics of hydrogen

[a] *National Renewable Energy Laboratory (NREL), 5013 Denver W Pkwy, Golden, CO 80401, USA. E-mail: mirjana.dimitrievska@nrel.gov, mirjana.dimitrievska@nist.gov*
[b] *NIST Center for Neutron Research, National Institute of Standards and Technology, Gaithersburg, MD 20899-6102, USA*
[c] *Pacific Northwest National Laboratory (PNNL), Richland, WA 99352, USA*
[d] *University of Hawaii Manoa, Department of Chemistry, Honolulu, HI 96822-2275, USA*

† Electronic supplementary information (ESI) available. CCDC 1963436 and 1963437. For ESI and crystallographic data in CIF or other electronic format see DOI: 10.1039/c9cp03311d

This journal is © the Owner Societies 2020

Published on 20 November 2019. Downloaded on 12/31/2019 8:06:50 PM.

desorption and absorption at low operating temperature and pressure, and a high purity of the released hydrogen are the most important. Promising alternatives for hydrogen storage include carbon nanostructures,[2,3] liquid organic hydrogen carriers,[4] metal organic frameworks[5] and complex borohydrides.[6]

Metal borohydrides [$M(BH_4)_n$] are considered as attractive materials for hydrogen storage applications due to their high volumetric and gravimetric hydrogen densities. $M(BH_4)_n$ are largely ionic compounds composed of tetrahedral hydrogen-rich molecular BH_4^- anions counterbalanced by metal cations, M^{n+}. Among the alkali- and alkaline-earth-based borohydrides, magnesium borohydride [$Mg(BH_4)_2$] displays very interesting properties both from fundamental and application points of view. $Mg(BH_4)_2$ has a more favorable thermodynamic stability in comparison to, *e.g.*, $LiBH_4$, while still maintaining attractive hydrogen storage capacities of 14.9 mass%.[7,8] However, the reaction kinetics of $Mg(BH_4)_2$, which is still not fully understood, along with its decomposition pathways occurring in a multi-step process only at 600 K,[9,10] and its limited reversibility,[11] make $Mg(BH_4)_2$ still unsuitable for practical applications.

Recently, different additives have been used in order to enhance the kinetics of hydrogen release from $Mg(BH_4)_2$.[12–15] These studies have found that the onset temperature of hydrogen release could be reduced upon addition of metal fluorides[13–15] or by mechanically milling $Mg(BH_4)_2$ with TiO_2.[15] Additionally, accelerated thermal dehydrogenation of $Mg(BH_4)_2$ was observed in mixtures with $LiBH_4$.[16–18]

Several studies have also suggested that adducts of $Mg(BH_4)_2$ complexed with solvent molecules might lead to beneficial enhancements in hydrogen kinetics.[19–23] Among these, adducts with tetrahydrofuran (THF = C_4H_8O) have proven to be especially interesting, as it was found that THF binds to the Mg^{2+} and appears to modify its chemistry, increasing both selectivity and kinetics for H_2 release (and reversible uptake).[23] However, the specific role of THF in the hydrogenation and dehydrogenation process is still ambiguous, and as such, in-depth foundational studies of the THF interactions with BH_4^- and Mg^{2+} may provide further insight.

Investigating physicochemical properties of $Mg(BH_4)_2{\cdot}x$THF adducts constitutes a challenge from an experimental point of view, as selectivity to different components, *e.g.*, BH_4^- and THF, is required. Neutron scattering techniques are invaluable in this case, as they offer selectivity to a given component through isotopic (H/D) labeling. In the case of incoherent neutron scattering techniques (neutron vibrational spectroscopy (NVS) and quasielastic neutron scattering (QENS)) related to hydrogen self-motions, deuteration can significantly reduce the scattered intensity, thereby masking the deuterated component to neutrons. Additionally, QENS also provides space/time resolution at a molecular level through the momentum transfer dependence of the magnitudes measured. On the other hand, structural information, which is crucial for the understanding of vibrational and dynamical results, can be provided from neutron powder diffraction (NPD) measurements.

This work focuses on exploring the structural, vibrational, and dynamical properties of the THF-rich $Mg(BH_4)_2{\cdot}3$THF adduct through neutron-scattering methods and molecular DFT calculations. Some additional limited experimental and theoretical comparisons with $Mg(BH_4)_2$ and the relatively THF-poorer $2Mg(BH_4)_2{\cdot}$THF adduct provide further insights concerning the dependences of BH_4^- and THF dynamics on adduct stoichiometry. In some experiments, selective masking of the THF molecules within the $Mg(BH_4)_2{\cdot}x$THF adducts *via* their deuteration allowed us to isolate and characterize more effectively the individual behaviors of the BH_4^- anions and THF molecules.

Experimental details

Materials

To facilitate neutron scattering measurements, all samples were prepared using ^{11}B-enriched $Mg(^{11}BH_4)_2$ from Katchem[24] as a starting material; this leads to a significant reduction of the neutron absorption otherwise due to the ^{10}B isotope in natural boron. Moreover, for some neutron scattering measurements, where appropriate, synthesized adducts with fully deuterated THF (*i.e.*, TDF) were used.

Sample preparation and storage were conducted either in a nitrogen glovebox or on a Schlenk line. The solvents were dried over molecular sieves and verified by NMR for purity before use.

Two $Mg(BH_4)_2{\cdot}x$THF adduct stoichiometries were prepared with THF/$Mg(BH_4)_2$ stoichiometric ratios x = 3 and 0.5, as previously described in ref. 23. Briefly, diethyl ether was added to a round-bottom flask containing 400 mg of α-phase $Mg(BH_4)_2$ until the borohydride was dissolved. In a subsequent step, a stoichiometric quantity, 0.5 or 3 equivalents of THF or TDF per $Mg(BH_4)_2$, was added by a micropipette to the ether solution at room temperature and stirred for 30 min. The excess ether was then removed *in vacuo* at room temperature for 12 hours to yield the THF adducts of $Mg(BH_4)_2$. This vacuum treatment did not remove THF, since prolonged exposure of $Mg(BH_4)_2{\cdot}3$THF under vacuum did not change its stoichiometry or crystallinity.

Room-temperature XRD data for $Mg(BH_4)_2{\cdot}3$THF confirmed the formation of the known monoclinic structure. The indexing of comparable XRD data for the more THF-deficient $2Mg(BH_4)_2{\cdot}$THF (*i.e.*, x = 0.5) also suggested primarily a single phase with monoclinic symmetry but of as-of-yet unknown structure and exact stoichiometry.

Methods

All neutron scattering measurements were performed at the National Institute of Standards and Technology Center for Neutron Research using 0.5 g of each powdered sample mounted in a thin-walled annular geometry (5 cm height × 1.2 cm annulus diameter) inside a He-filled, indium o-ring-sealed, cylindrical Al sample cell.

Neutron powder diffraction (NPD) measurements were performed between 5 K and 300 K using the BT-1 High-Resolution Neutron Powder Diffractometer[25] with the Cu(311) monochromator at λ = 1.5397(2) Å and an in-pile collimation of 60 min of arc.

Published on 20 November 2019. Downloaded on 12/31/2019 8:06:50 PM.

Neutron vibrational spectroscopy (NVS) measurements were performed at 4 K using the Filter-Analyzer Neutron Spectrometer (FANS)[26] with both the Cu(220) and pyrolytic graphite PG(002) monochromators and pre- and post-collimations of 20′ of arc, yielding a full-width-at-half-maximum (fwhm) energy resolution of about 3% of the neutron energy transfer. QENS measurements were performed up to 315 K using two complementary instruments: the Disc Chopper Spectrometer (DCS)[27] between 4 K and 315 K using an incident neutron wavelength (λ) of 4.5 Å, 10 Å and 12 Å with respective fwhm resolutions of 67 μeV, 17 μeV and 10.9 μeV and respective maximum attainable elastic scattering vector (Q) values of around 2.62 $Å^{-1}$, 1.18 $Å^{-1}$ and 0.98 $Å^{-1}$; and the High Flux Backscattering Spectrometer (HFBS)[28] between 4 K and 315 K [plus up to 350 K during an elastic-scattering fixed-window scan (FWS)] using an incident neutron wavelength of 6.27 Å (2.08 meV) with a fwhm resolution of 0.8 μeV and a maximum attainable Q value of 1.75 $Å^{-1}$. Instrumental resolution functions were determined from QENS spectra at lower temperatures free of quasielastic scattering, *i.e.*, at 4 K. QENS data were analyzed using the DAVE software package.[29]

Solid-state density-functional theory (DFT) calculations were performed using the Quantum-Espresso package.[30] A cutoff energy of 544 eV and a 2 × 2 × 1 k-point mesh (generated using the Monkhorst–Pack scheme) were used and found to be enough for the total energy to converge within 0.01 meV per atom. Crystal structures were first fully optimized, based on the experimental structures, and are presented in the ESI.† For comparison with the NVS measurements, simulated phonon densities of states (PDOSs) were generated from the DFT-optimized structures using the supercell method (2 × 2 × 1 cell size) with finite displacements (0.02 Å) and were appropriately weighted to take into account the total neutron scattering cross sections of the different elements. Gas phase DFT calculations were done using the B3LYP functional[31–34] and the Gaussian 6-31+G* basis set[35,36] to calculate the binding energies of the 1st, 2nd and 3rd THF molecules to $Mg(BH_4)_2$. The optimized geometries were verified by the absence of imaginary frequencies from the frequency analysis in the harmonic oscillator/rigid-rotor approximation. The frequencies were also used to calculate the enthalpic and entropic contributions to the free energy for binding. All calculations were done using the NWChem software.[37]

Structural depictions were made using the VESTA (Visualization for Electronic and Structural Analysis) software.[38] For all figures, standard uncertainties are commensurate with the observed scatter in the data, if not explicitly designated by vertical error bars.

Results and discussion

Structural behavior and vibrational dynamics of $Mg(BH_4)_2$·3THF

Neutron powder diffraction measurements of the partially deuterated sample, $Mg(BH_4)_2$·3TDF, upon heating from 5 K to 298 K indicate a phase transition in the temperature range between 175 and 225 K, as shown in Fig. 1. Prior low-temperature (100 K) and room-temperature (298 K) XRD measurements of $Mg(BH_4)_2$·3THF suggested two crystalline forms of this material

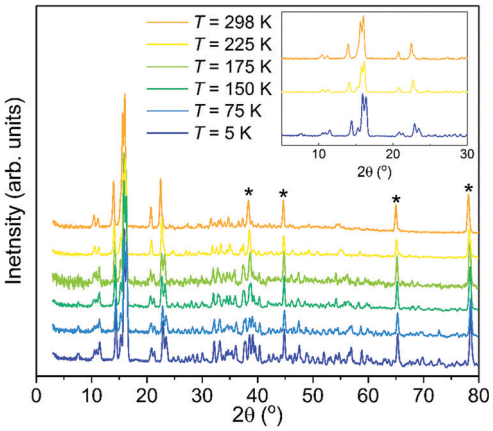

Fig. 1 Progression of NPD patterns [λ = 1.5397 Å] of $Mg(BH_4)_2$·3TDF with temperature, upon heating from 5 K to 298 K, showing the structural transformation from triclinic $P\bar{1}$ symmetry to monoclinic $C2/c$ symmetry. The inset shows patterns at 5 K, 225 K, and 298 K for clarity to distinguish from the intervening patterns measured at other temperatures. Asterisks mark the reflections obtained from the Al container.

with triclinic (space group $P\bar{1}$)[39] and monoclinic (space group $C2/c$)[40] structures, respectively. To confirm these structures, Rietveld refinements of the NPD patterns (at 298 K and 225 K) above and (at 5 K) below this phase transition were performed. The analysis corroborated a lowering of the symmetry upon decreasing the temperature, from monoclinic $C2/c$ to $P\bar{1}$ *via* a triclinic distortion from respective α, β, and γ values of 90°, 144.992(4)°, and 90° at 298 K to 102.596(3)°, 103.984(4)°, and 92.239(3)° at 5 K. Fig. S1 in the ESI† presents the model refinements of the NPD data at 298 K, 225 K, and 5 K. Table S1 and supplemental CIF files, also in the ESI,† summarize the structural analysis details. It should be noted that the lattice parameters from ref. 40 were associated with a different unit cell convention than that used in this paper. Converting these parameters to the present convention yield values of a = 12.120 Å, b = 12.646 Å, c = 20.216 Å, and β = 144.96°, which are in good agreement with our values. We note that the slightly smaller lattice constants associated with the present results are consistent with the incorporation of TDF, instead of THF, in our NPD samples. Molecular vibrational amplitudes associated with deuterated molecules are somewhat smaller than their hydrogenated analogues, leading to slightly less space required to accommodate the former molecules compared to that for the latter.

Fig. 2 shows the molecular and crystal structures of the low- and room-temperature $Mg(BH_4)_2$·3TDF phases. It is apparent that the packing of molecules in both crystalline forms takes place in a layered lattice, with interchangeable layers of BH_4^- anions and TDF rings. The three TDF molecules and two BH_4^- anions are located around the central Mg^{2+} cation in a trigonal bipyramidal motif. The BH_4^- anions are bonded to the Mg^{2+} cation *via* double hydrogen bridges. The coordination polyhedron of Mg^{2+} can be described by a distorted pentagonal-bipyramidal geometry, where the axial vertices are occupied by the O atoms of the two apical TDF rings, while the four bridging H atoms from the BH_4^- anions and the O atom from the third TDF ring lie

 This journal is © the Owner Societies 2020

Published on 20 November 2019. Downloaded on 12/31/2019 8:06:50 PM.

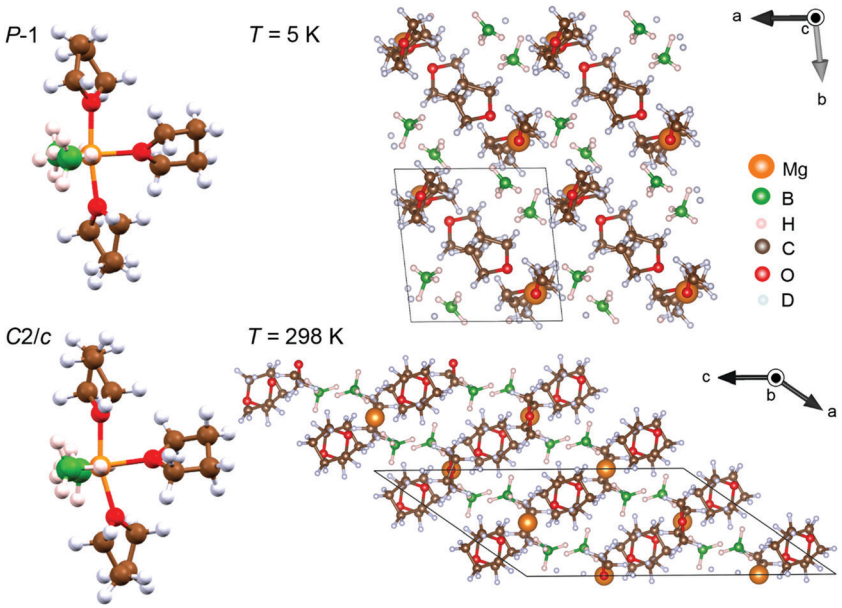

Fig. 2 Molecular and crystal structures of the low-temperature ($P\bar{1}$ symmetry) and room-temperature ($C2/c$ symmetry) $Mg(BH_4)_2{\cdot}3TDF$ phases.

mostly in the equatorial plane. The detachment of the apical TDF rings from the BH_4^- anions is observed from the O–Mg–O angles of 172.1° and 163.6° in the respective $P\bar{1}$ and $C2/c$ structures, as well as from the slightly longer Mg–O distances to the apical TDF molecules. However, the arrangement of the Mg, O, and two B atoms in the equatorial plane is perfectly coplanar, with low deviations from the ideal angle of 120° in a trigonal bipyramidal coordination geometry. Higher values of the B–Mg–B angle in comparison to both B–Mg–O angles are observed due to a more repulsive force between the negatively charged BH_4^- anions than between the coordinated TDF ring and BH_4^- anion. No significant distortion of the TDF rings or BH_4^- anions has been observed in either crystalline form, with bond lengths and bond angles not being different from the expected values.[41] However, the interatomic Mg and B separations of 2.49 Å in $P\bar{1}$ and 2.46 Å in $C2/c$ are slightly greater than 2.41 Å reported for pristine α-$Mg(BH_4)_2$.[41]

The neutron vibrational spectra for $Mg(BH_4)_2{\cdot}3THF$ and $Mg(BH_4)_2{\cdot}3TDF$ at 4 K based on FANS measurements are shown in Fig. 3 and compared with the simulated phonon density of states (PDOS) from the DFT-optimized triclinic structure, indicating overall good agreement between experiment and theory. Further information about the character, symmetry, and energies of the different phonon modes contributing to the simulated PDOSs can be found in the ESI.†

Upon comparison of the $Mg(BH_4)_2{\cdot}3THF$ NVS spectrum with that of pristine α-$Mg(BH_4)_2$, obvious peak splitting in the lower frequency region (<80 meV) is observed. This is mostly due to the coordination of THF rings, which affects the bonding between the Mg atoms and BH_4^- anions. Based on the structural data, the presence of THF rings causes extension of the interatomic distance between the Mg and B atoms and reduction in the B–Mg–B angle in comparison to the pristine α-$Mg(BH_4)_2$.

Direct comparison between NVS spectra of $Mg(BH_4)_2{\cdot}3THF$ and $Mg(BH_4)_2{\cdot}3TDF$, as well as the mode identification obtained from the DFT PDOS calculations, can help distinguish the modes dominated by the vibrational displacements of the BH_4^- anions and those of the THF molecules. This is due to the fact that, while the TDF spectrum by itself is measurable, as can be seen in Fig. 3, its overall contribution to the $Mg(BH_4)_2{\cdot}3TDF$ spectrum is very small, thus accentuating the BH_4^- contributions. Additionally, it should be mentioned that the noticeable shift in peak positions between the crystalline THF and TDF compounds is due to the mass difference between H and D atoms, where heavier D atoms cause peak-shifting to lower energy transfer.

By analyzing the spectra in this way, it can be seen that most peaks observed in the low-energy region from 20 to 65 meV (1 meV ≈ 8.066 cm^{-1}) for $Mg(BH_4)_2{\cdot}3THF$ in Fig. 3 correspond to the BH_4^- librational (torsional) modes.[42] Moving to higher energy-transfer values, two sharp features are observed at around 70 and 84 meV, and are attributed to vibrations related to THF ring deformations and CH_2 wagging.[43] Furthermore, a number of sharp peaks are noticeable in the 100–190 meV spectral region of $Mg(BH_4)_2{\cdot}3THF$, of which eight peaks centered at around 107, 114, 120, 128, 144, 154, 167 and 182 meV are particularly intense. According to group-theory calculations,[44,45] BH_4^- anions have a high tetrahedral (T_d) symmetry for which the irreducible representation in the Mulliken notation can be written as $\Gamma = A_1 \oplus E \oplus 2F_2$, while THF rings have two-fold rotational (C_2) symmetry with the irreducible representation given as $\Gamma = 17A \oplus 16B$. Here, the A and B modes are non-degenerate, while the E modes are doubly degenerate, and the F modes are triply degenerate. Having in mind this notation and comparing the results with the DFT simulations and the experimental spectra of pristine α-$Mg(BH_4)_2$, THF, and TDF, the very intense peaks observed in the 100–190 meV region could be resolved as follows: the peaks observed at 144 and 154 meV mostly correspond to the asymmetric bending vibrations of BH_4^- (F_2 symmetry mode), while the peaks at 167 and 183 meV are attributed to the

Published on 20 November 2019. Downloaded on 12/31/2019 8:06:50 PM.

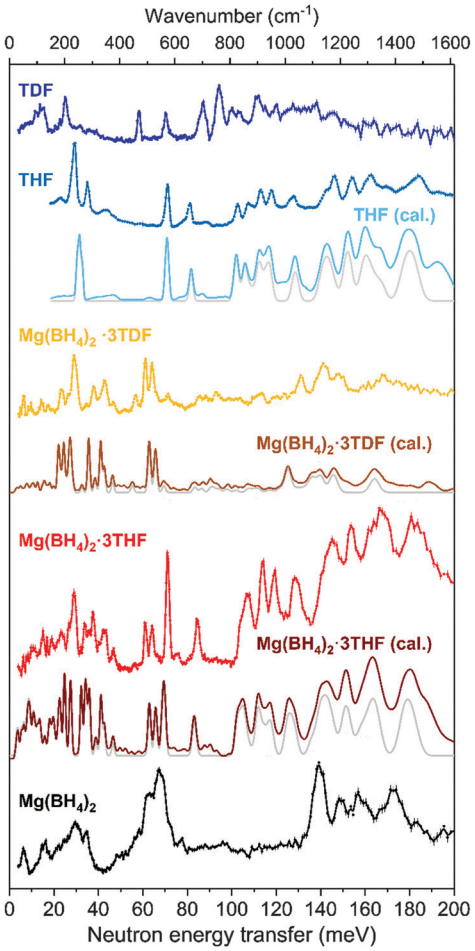

Fig. 3 Neutron vibrational spectra for $Mg(BH_4)_2{\cdot}3THF$ (red) and $Mg(BH_4)_2{\cdot}3TDF$ (orange) at 4 K compared with the simulated 0 K 1-phonon- (light gray) and 1+2-phonon-density-of-states spectra (dark red and brown) after DFT energy optimization of the triclinic $P\bar{1}$-symmetric structure derived from the 5 K NPD data. Neutron vibrational spectra of pristine α-$Mg(BH_4)_2$ (black), THF (blue), and TDF (dark blue), as well as the simulated 0 K 1-phonon- (light gray) and 1+2-phonon-density-of-states spectrum (light blue) of THF are shown for reference and comparison. The Cu(220) and pyrolytic graphite (002) monochromators were used above and below 40 meV, respectively. Vertical error bars denote $\pm 1\sigma$.

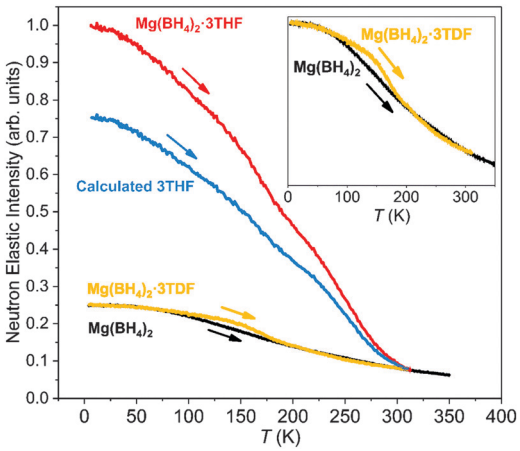

Fig. 4 Scaled neutron-elastic-scattering fixed-window scans (FWSs) (upon heating at 0.5 K min^{-1}) for $Mg(BH_4)_2{\cdot}3THF$ and $Mg(BH_4)_2{\cdot}3TDF$ measured between 4 K and 315 K, at Q = 0.87 $Å^{-1}$ with 0.8 μeV fwhm instrumental resolution on HFBS. FWS of pristine β-$Mg(BH_4)_2$ was measured as a reference in a similar temperature region, from 4 K to 350 K under the same conditions. The scan labeled "Calculated 3THF" was obtained by subtracting the FWS of $Mg(BH_4)_2{\cdot}3TDF$ from that of $Mg(BH_4)_2{\cdot}3THF$ using the procedure explained in the text. Inset shows zoomed comparison of the FWSs from $Mg(BH_4)_2{\cdot}3TDF$ and α-$Mg(BH_4)_2$.

symmetric bending vibrations of BH_4^- (E symmetry mode). The lower energy peaks at 107, 114, 120, 128, 144 meV are related to the A and B modes of THF, corresponding mostly to stretching vibrations.

Reorientational dynamics of $Mg(BH_4)_2{\cdot}3THF$

The neutron-elastic-scattering fixed-window scan (FWS) presents a plot of the temperature dependence of the neutron scattering intensity at zero energy transfer. As such, a direct comparison of the FWSs measured from the different compounds provided some insights into the reorientational dynamics of the THF and BH_4^- groups in these materials. Fig. 4 shows the FWS for $Mg(BH_4)_2{\cdot}3THF$ and $Mg(BH_4)_2{\cdot}3TDF$ measured on HFBS at Q = 0.87 $Å^{-1}$ between 4 K and 315 K [limited by the decomposition temperature of $Mg(BH_4)_2{\cdot}3THF$]. The FWS for pristine α-$Mg(BH_4)_2$ was measured as a reference in a similar temperature region, from 4 K to 350 K. Again, due to the much lower incoherent neutron scattering cross section of D in comparison to H, the contribution of TDF molecules to the FWS could be neglected (to first order), allowing for all FWSs to be scaled according to their number of H atoms. The FWS of $Mg(BH_4)_2{\cdot}3THF$, with a total of 32 H atoms, was normalized to 1 at the lowest temperature, while FWS plots of $Mg(BH_4)_2{\cdot}3TDF$ and α-$Mg(BH_4)_2$, with a total of 8 H atoms each, were scaled to 1/4 of the value of $Mg(BH_4)_2{\cdot}3THF$ at the lowest measured temperature of 4 K. Assuming that the FWS for $Mg(BH_4)_2{\cdot}3TDF$ reflects only the dynamical contributions of the BH_4^- anions allows the estimation of the dynamical contributions solely from the three THF molecules in $Mg(BH_4)_2{\cdot}3THF$ (labeled in Fig. 4 as "Calculated 3THF") by subtracting the FWS of $Mg(BH_4)_2{\cdot}3TDF$ from that of $Mg(BH_4)_2{\cdot}3THF$.

Upon heating from 4 K, a fall-off in intensity with increasing temperature occurs for all scans depicted in Fig. 4, reflecting the composite Debye–Waller-type hydrogen vibrational displacements associated with the THF and BH_4^- groups. Above certain threshold temperatures (at around 230 K for THF and 160 K for BH_4^- in the adducts) the fall-offs accelerate, signaling that THF and BH_4^- reorientational jumps are coming into the HFBS resolution window with frequencies beginning to exceed 10^7–10^8 s^{-1}. As temperatures further increase, the fall-off in intensity begins to slow again, signaling that the reorientational jump frequencies are now approaching the order of 10^{10} s^{-1} and moving out of the HFBS dynamic range window. For $Mg(BH_4)_2{\cdot}3THF$, this seems to occur above around 300 K for THF and 190 K for BH_4^-.

Comparison of the FWSs from $Mg(BH_4)_2{\cdot}3TDF$ and pristine α-$Mg(BH_4)_2$, presented in the inset in Fig. 4, shows differences in the slopes of the two curves in the lower-temperature region, up to 200 K, leading to the conclusion that the BH_4^- anions in $Mg(BH_4)_2{\cdot}3TDF$ have lower reorientational mobilities compared to the BH_4^- anions in $Mg(BH_4)_2$ at the same temperature in

 This journal is © the Owner Societies 2020

Published on 20 November 2019. Downloaded on 12/31/2019 8:06:50 PM.

this region. However, above 200 K, BH_4^- anions in both compounds behave the same, based on the overlap of the FWS plots. The drastic change of the reorientational mobilities of the BH_4^- anions in the 200 K temperature region coincides with the triclinic to monoclinic structural phase transition for $Mg(BH_4)_2$·3TDF, as explained previously by the NPD experiments. Additionally, the noticeable change in slope above about 175 K for the FWS component intensity for THF in $Mg(BH_4)_2$·3THF likely marks a change in the Debye–Waller factor for THF due to this same phase transition.

Complementary QENS measurements on the DCS and HFBS instruments were undertaken to gain further insights concerning the reorientational behavior of both THF and BH_4^- groups. Fig. 5 presents two exemplary QENS spectra for $Mg(BH_4)_2$·3TDF measured at (a) 280 K and (c) 200 K, and two spectra for $Mg(BH_4)_2$·3THF measured at (b) 267 K and (d) 290 K, on two instruments at different resolutions [(a) and (b) on HFBS with 0.8 μeV resolution; and (c) and (d) on DCS with 16.9 μeV resolution]. All QENS spectra were adequately fit with a delta function and a single Lorentzian component, both convoluted with the resolution function, above a flat background. For all temperatures, the width of the Lorentzian function, Γ, associated with each component group was found to be Q-independent over the measured Q-range (Fig. S2 in the ESI†), consistent with simple localized hydrogen jump motions[46] for both THF and BH_4^- groups, as opposed to long-range diffusive motions.

Fig. 6 conveys the Arrhenius-like dependencies between 160 K and 320 K of the fundamental jump correlation frequency $\tau_1^{-1} = \Gamma/(2\hbar)$ *vs.* T^{-1} for $Mg(BH_4)_2$·3TDF, $Mg(BH_4)_2$·3THF, and pristine α-$Mg(BH_4)_2$.

Similarities in the BH_4^- reorientational jumps for $Mg(BH_4)_2$·3TDF, $Mg(BH_4)_2$·3THF and unsolvated $Mg(BH_4)_2$ lead to the conclusion that the mobilities of the BH_4^- anions are not noticeably affected by the presence of THF rings in the higher-temperature region from 200 K to 320 K, displaying jump correlation frequencies of the order of 10^{10} to 10^{11} s^{-1}, in agreement with those previously reported in $Mg(BH_4)_2$.[47] Further lowering the temperature, from 200 K to 160 K, leads to a sudden 75% drop in the BH_4^- jump frequencies, compared to the trending values above 200 K. This decrease is explained by the phase transition of $Mg(BH_4)_2$·3TDF from the monoclinic to the triclinic structure with a smaller unit cell size, presumably leading to enhanced steric effects and thus smaller jump frequencies. This is further portrayed by the calculated activation energies for reorientations, E_a, (derived from the slope $(-E_a/k_B)$ of the linear fit to $\ln(\tau_{i1}^{-1})$ *vs.* T^{-1}), where a higher barrier is observed in the triclinic structure, *i.e.*, $E_a = 137(3)$ meV for $T \leq 200$ K, compared to the monoclinic structure with $E_a = 113(3)$ meV for $T > 200$ K.

The nature of the reorientational mechanism of the BH_4^- anions in $Mg(BH_4)_2$·3TDF and $Mg(BH_4)_2$·3THF was determined

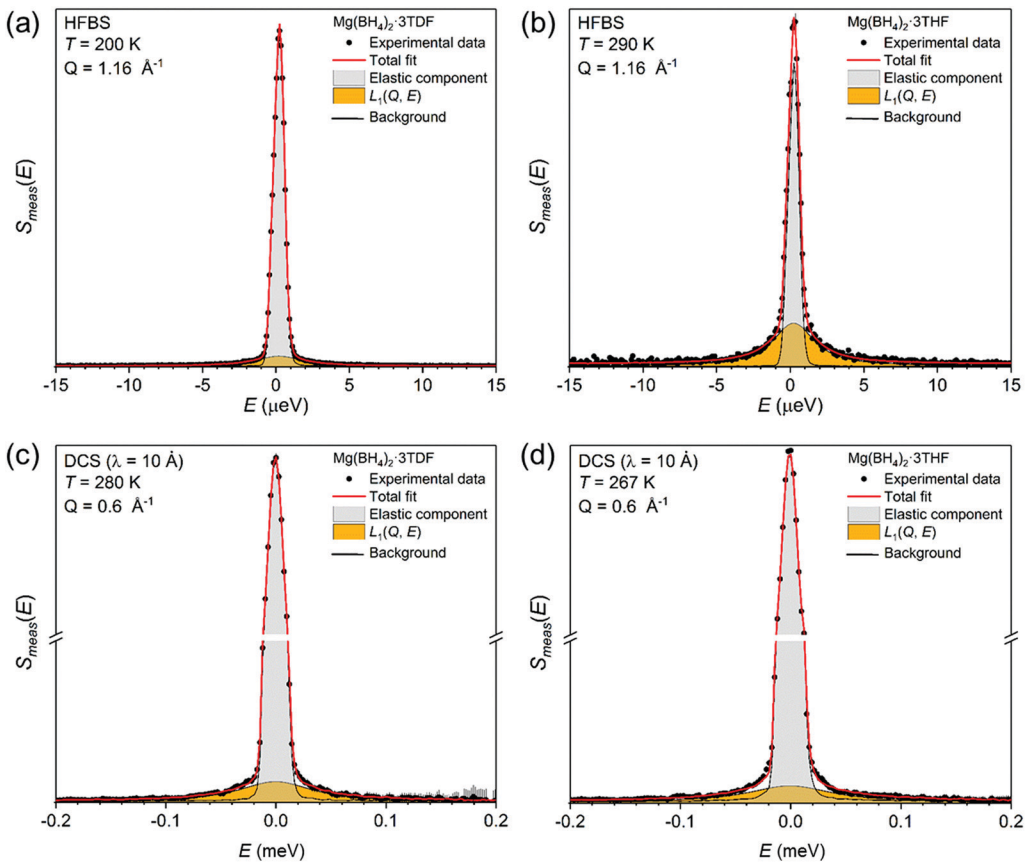

Fig. 5 QENS spectra measured on HFBS at Q = 1.16 $Å^{-1}$, 0.8 μeV resolution, for (a) $Mg(BH_4)_2$·3TDF at 200 K, and (b) $Mg(BH_4)_2$·3THF at 290 K. QENS spectra measured on DCS at Q = 0.6 $Å^{-1}$, 16.9 μeV resolution, for (c) $Mg(BH_4)_2$·3TDF at 280 K, and (d) $Mg(BH_4)_2$·3THF at 267 K.

Published on 20 November 2019. Downloaded on 12/31/2019 8:06:50 PM.

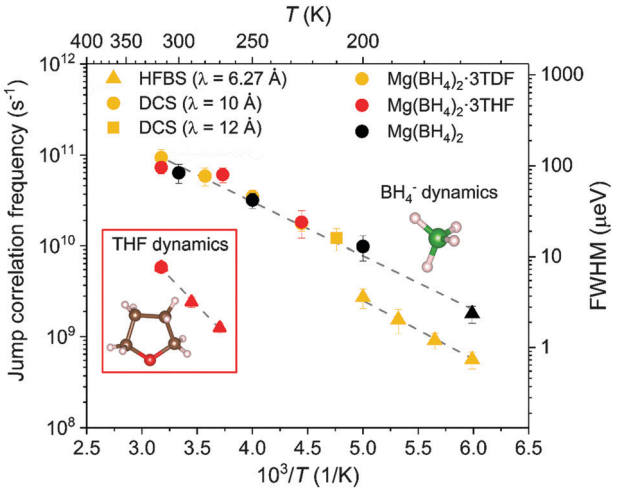

Fig. 6 Jump correlation frequency τ_{j1}^{-1} *vs.* inverse temperature for $Mg(BH_4)_2$·3TDF, $Mg(BH_4)_2$·3THF, and pristine $Mg(BH_4)_2$. Different symbols denote the different instruments used. Different colors denote the different samples. Dashed lines represent linear fits to the QENS data.

by the calculated Elastic Incoherent Structure Factor (EISF) over the large Q-range accessible with DCS and using 4.5 Å incident wavelength neutrons. Fig. 7 shows the experimentally derived EISF data at 315 K due solely to the BH_4^- anions in $Mg(BH_4)_2$·3TDF. Based on the invariant Lorentzian widths with Q, two possible localized hydrogen motions are expected in this system, rotations around any one of the three two-fold (C_2) or four three-fold (C_3) molecular symmetry axes of the BH_4^- units. For BH_4^- rotations around a C_2-axis, the tetrahedral anions have two equal equilibrium orientations, while for BH_4^- rotations around a C_3-axis, the tetrahedral anions have three equal equilibrium orientations, while one hydrogen atom remains immobile. In both cases, the final expression for the EISF is identical and given by:[46]

$$\mathrm{EISF}_{C_2/C_3}(\mathrm{BH_4^-}) = \frac{1}{2}(1 + j_0(Qd)) \qquad (1)$$

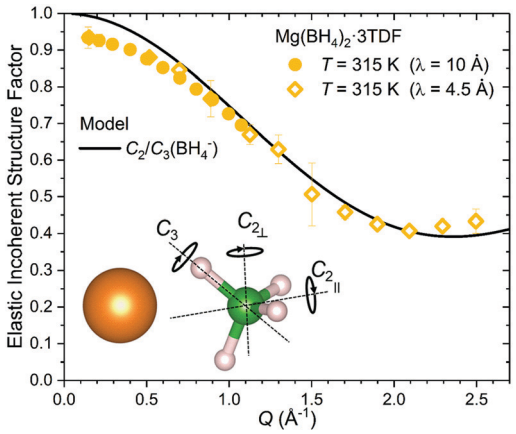

Fig. 7 The EISF for the BH_4^- anions in $Mg(BH_4)_2$·3TDF determined from 315 K DCS data (using 4.5 Å and 10 Å incident wavelength neutrons) compared with the model curve corresponding to uniaxial reorientations involving either two-fold or three-fold jumps of BH_4^- anions ($C_2/C_3(BH_4^-)$ model).

where $j_0(x)$ is a zeroth-order Bessel function equal to $\sin(x)/(x)$, and $d \approx 2.0$ Å is the jump distance between two BH_4^- hydrogen atom positions. Excellent agreement is seen between the plotted C_2/C_3 model and the experimental data at 315 K. (It should be noted that the minor deviations seen at lower Q-values are a signature of minor multiple-scattering effects due to a sample that is somewhat thicker than desired.) As the EISF by itself cannot distinguish between a C_2- or C_3-type jump mechanism for the BH_4^- anions, it is also necessary to consider the jump frequencies and the activation energies corresponding to this process. In principle, different jump frequencies and activation energies are expected for different types of reorientations of the same BH_4^- anion. The coordination of the BH_4^- anions in $Mg(BH_4)_2$·3TDF with respect to the Mg^{2+} cations is similar to that in unsolvated $Mg(BH_4)_2$ compounds, namely, the BH_4^- anions are oriented toward the Mg^{2+} cations roughly along a molecular two-fold symmetry axis so that the Mg^{2+} cations are straddled by two of the four BH_4^- hydrogen atoms. Although the Mg^{2+}–BH_4^- bond distances are also similar among the solvated and unsolvated compounds, the structures differ somewhat in that each BH_4^- anion in unsolvated $Mg(BH_4)_2$ is in nearly linear coordination with two near-neighbor Mg^{2+} cations, whereas each BH_4^- anion in $Mg(BH_4)_2$·3TDF coordinates to only one Mg^{2+} cation (see Fig. 7). This coordinative arrangement suggests that the rotation around the particular two-fold symmetry axis that is roughly parallel with that connecting B and Mg atoms (horizontal C_2-axis in Fig. 7) does not break any Mg–H bonds. Thus, this type of motion is expected to have a lower activation energy than the rotation around the two other two-fold symmetry axes of the BH_4^- anion, which breaks all Mg–H bonds, or, the rotation around any of the three-fold symmetry axes (one of which is shown as C_3 in Fig. 7), which breaks half of the Mg–H bonds. The activation energy and the jump frequencies measured for $Mg(BH_4)_2$·3TDF and $Mg(BH_4)_2$ in this case compare well with the values obtained by the recent NMR measurements for $Mg(BH_4)_2$ (E_a = 116(6) meV and $\tau_1^{-1} = 1.5 \times 10^8$ s^{-1} at 170 K),[48] which correspond to the rotation around the two-fold axis connecting B and Mg atoms. Therefore, the most likely mechanism in the present case for the BH_4^- anions in $Mg(BH_4)_2$·3TDF involves two-fold jumps around the symmetry axis nearly parallel to that connecting B and Mg atoms (C_2 model). Additionally, based on the EISF dependence with temperature for $Mg(BH_4)_2$·3TDF, no differences in the reorientational mechanisms are observed upon the phase transition from a monoclinic to triclinic structure.

Another type of dynamics could be identified from Fig. 6, observed from the HFBS measurements of $Mg(BH_4)_2$·3THF. Order-of-magnitude-slower jump correlation frequencies, in the range of 10^9 s^{-1} to 10^{10} s^{-1}, when compared to BH_4^- anions at the same temperature, could be attributed to the localized hydrogen motion associated with the THF rings. This is further confirmed by investigating possible reorientational mechanisms of the THF molecules in $Mg(BH_4)_2$·3THF and comparing with the experimentally obtained EISF.

Due to the C_2 symmetry of the THF ring and the Q-independent Lorentzian widths obtained from the QENS fitting of $Mg(BH_4)_2$·3THF measured on the HFBS instrument, the only

 This journal is © the Owner Societies 2020

Published on 20 November 2019. Downloaded on 12/31/2019 8:06:50 PM.

possible localized motion of H atoms involves two-fold jumps around the anchored C_2-axis, which passes through the O atom and the middle of the opposite C–C bond within the THF ring [C_2(THF) model]. Such THF reorientations involve much larger moments of inertia than for BH_4^- reorientations, since the former also require the jump displacements of the C atoms. In this case, the EISF is given as:

$$\mathrm{EISF}_{C_2}(\mathrm{THF}) = \frac{1}{2} + \frac{1}{8}\cdot\left(j_0(Q\cdot d_1) + j_0(Q\cdot d_2) + j_0(Q\cdot d_3) + j_0(Q\cdot d_4)\right) \quad (2)$$

where d_1 = 2.89 Å, d_2 = 2.57 Å, d_3 = 3.70 Å and d_4 = 3.89 Å are distances between the exchanging H atoms, as shown in Fig. S3 in the ESI.†

Considering that the BH_4^- anions have an active dynamical behavior in the measured temperature range, the EISF associated with the BH_4^- anions should also be included in the calculation of the total EISF for $Mg(BH_4)_2{\cdot}3THF$. The total EISF is calculated by including the weighting factors based on the number of H atoms in front of the EISF of each chemical group. Considering that there are a total of 32 H atoms, with 24 present in the three THF rings, and 8 present in the two BH_4^- anions, the total EISF is given as:

$$\mathrm{EISF(total)} = \frac{24}{32}\cdot\mathrm{EISF}_{C_2}(\mathrm{THF}) + \frac{8}{32}\cdot\mathrm{EISF}_{C_2/C_3}(\mathrm{BH_4^-}). \quad (3)$$

In the HFBS data measured, the elastic peak contribution is actually the sum of the elastic peak intensities due to both THF and BH_4^- reorientations, whereas the fitted quasielastic contribution is due only to the slower THF reorientations. The much faster BH_4^- reorientations yield quasielastic scattering that is an order of magnitude too broad to be observed by HFBS and resides as broad background scattering buried under the flat baseline. In order to extract the EISF solely due to the THF molecules, it is necessary to determine the amount of THF elastic scattering intensity by calculating and subtracting the BH_4^- elastic scattering intensity from the total elastic scattering measured. This can be done with the aid of eqn (3) and the fact that the EISF behavior for the BH_4^- anions is known. The mathematical details are outlined in the ESI.† The resulting experimental EISF for THF reorientations in $Mg(BH_4)_2{\cdot}3THF$ at 315 K is shown in Fig. 8 and is in good agreement with the theoretically predicted EISF from eqn (2) for two-fold THF jumps. The very different Q-dependent behavior of the comparative EISF plot for BH_4^- reorientations in Fig. 8 provides further corroboration that we are indeed observing two-fold THF reorientations in the HFBS data.

Effect of THF concentration on $Mg(BH_4)_2{\cdot}x$THF properties

The structural results show that THF is bound to the Mg^{2+} cation and there is little direct interaction between THF and the BH_4^- anion at the investigated temperatures. With three THF molecules bound to each Mg^{2+} cation, it is tempting to predict that the interactions between the Mg^{2+} cation and the BH_4^- anion will be weaker in THF-containing compounds. It is therefore surprising that no measurable change was observed

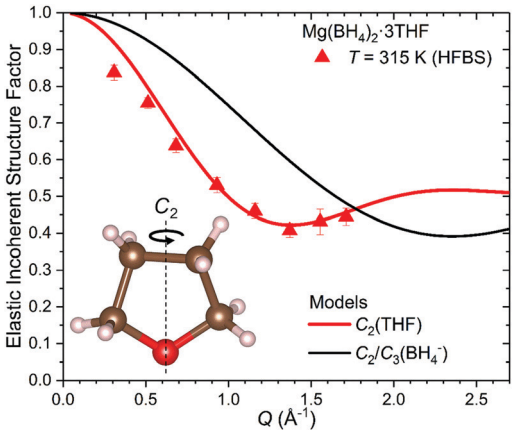

Fig. 8 The derived EISF for the THF molecules in $Mg(BH_4)_2{\cdot}3THF$ determined from 315 K HFBS data matched with the model curve (red) corresponding to uniaxial two-fold jumps [C_2(THF)]. The EISF (black) corresponding to uniaxial two- or three-fold jumps of BH_4^- anions [$C_2/C_3(BH_4^-)$] is shown for comparison.

in the rotational dynamics of the BH_4^- anion between the unsolvated α-$Mg(BH_4)_2$ and the solvated $Mg(BH_4)_2{\cdot}3THF$ adduct.

One possible explanation for this is the asymmetry in the Mg^{2+}–BH_4^- alignment that arises in the THF adducts. In unsolvated α-$Mg(BH_4)_2$, the BH_4^- anions sit approximately equidistant between two Mg^{2+} cations, with distances of around 2.41 Å and are oriented such that one of their C_2 anion symmetry axes is effectively aligned with the Mg–B–Mg bond direction. In $Mg(BH_4)_2{\cdot}3THF$, the Mg–B distance is slightly larger, 2.46–2.49 Å, but each BH_4^- anion only interacts with one Mg^{2+} cation. The next-nearest Mg^{2+} is more than 6 Å away. One would expect that this decreased Mg^{2+}–BH_4^- interaction, arising from the competing Mg^+–THF coordination and evidenced by a larger Mg–B distance would lead to an enhanced BH_4^- orientational mobility compared to that in $Mg(BH_4)_2$. Yet, in the $Mg(BH_4)_2{\cdot}3THF$ crystal structure, the Mg–B bond direction is not as well aligned with the corresponding BH_4^- C_2 symmetry axis (see Fig. 7) as in the unsolvated compound. Because of this misalignment, one can expect more steric interference with the adjacent Mg^{2+} cation while performing the BH_4^- two-fold reorientation. The counterpositioning of these two opposing effects on BH_4^- mobility may indeed result in similar BH_4^- reorientational dynamics for $Mg(BH_4)_2$ and $Mg(BH_4)_2{\cdot}3THF$ as observed. This is also corroborated by the fact that the BH_4^- librational energy around this easy C_2-axis in $Mg(BH_4)_2{\cdot}3THF$ is located between 25 meV and 28 meV by the DFT PDOS calculations and NVS experiments, which is very similar to the calculated and observed BH_4^- librational energy around the Mg–B–Mg axes in unsolvated $Mg(BH_4)_2$ phases.[42] Hence, it is not unreasonable to expect the corresponding rotational potential wells and dynamics to also be similar.

In addition to the observed BH_4^- mobility, one can speculate that a relatively weak Mg^{2+}–THF interaction in $Mg(BH_4)_2{\cdot}3THF$ is one key factor for enabling the THF rings to be orientationally mobile, undergoing 180° reorientational jumps around their C_2

Published on 20 November 2019. Downloaded on 12/31/2019 8:06:50 PM.

molecular symmetry axis. In order to explore this proposition further, molecular DFT calculations and additional QENS and NVS experiments were conducted for samples with a lower amount of THF present in the adduct. DFT calculations for $Mg(BH_4)_2{\cdot}THF$, $Mg(BH_4)_2{\cdot}2THF$ and $Mg(BH_4)_2{\cdot}3THF$ isolated clusters showed a slight lengthening of the Mg–O distance with each additional THF molecule that coordinates to the Mg^{2+} cation. The calculated Mg–O distance for the $Mg(BH_4)_2{\cdot}THF$ adduct is 2.06 Å, whereas addition of a second THF results in a symmetric structure with two Mg–O distances of 2.11 Å. Adding the third THF molecule results in further distancing of the THF molecules from Mg^{2+} and bond distances of 2.15–2.17 Å. Fig. 9 presents the zero-point corrected electronic energies calculated based on the gas-phase reference models for all compounds, which correspond more closely to low-temperature conditions. The calculated energies show that the first THF molecule binds most strongly with -85.7 kJ mol^{-1}, the second one binds with -60.7 kJ mol^{-1}, and the third one binds with -23.0 kJ mol^{-1} (Table S2 in the ESI†). Absolute energies and geometries of the structures are provided in Tables S3 and S4 in the ESI.† We expect that the simplicity of the molecular model and its treatment in the gas phase introduce entropic inaccuracies, and as such, result in positive binding free energies. However, because the DFT treatment is consistent for each addition reaction, we can reliably estimate the relative weakening in the binding energy for each subsequent THF molecule. This observation suggests that the reorientational dynamics of the THF rings may be more hindered in a material with a lower amount of solvent present. Indeed, comparative QENS measurements on the samples with the substoichiometric compositional ratio $2Mg(BH_4)_2{\cdot}THF$ and $2Mg(BH_4)_2{\cdot}TDF$ have shown no observable reorientational dynamics of the THF rings within the resolution window of the spectrometer (Fig. S4 in the ESI†), which is in line with a stronger binding energy of the THF rings to the Mg^{2+} cations. Additionally, no noticeable changes in the H dynamics of the BH_4^- anions are observed in this case either (Fig. S5 in the ESI†), leading to the conclusion that the THF solvent does not seem to appreciably affect the BH_4^- dynamical behavior in $Mg(BH_4)_2{\cdot}x$THF adducts. (Comparative NVS spectra of these substoichiometric compounds are provided in Fig. S6 in the ESI.†)

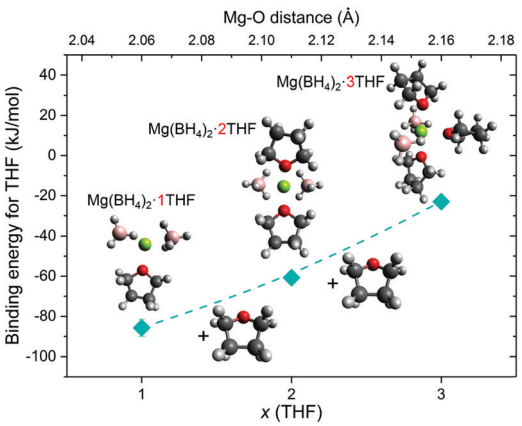

Fig. 9 THF binding energies for $Mg(BH_4)_2{\cdot}THF$, $Mg(BH_4)_2{\cdot}2THF$ and $Mg(BH_4)_2{\cdot}3THF$ obtained from the molecular DFT calculations. Red, green, pink, dark gray, and light gray spheres denote the respective O, Mg, B, C and H atoms.

The presence of a much stronger interaction between the THF and the Mg^{2+} cation for lower THF/$Mg(BH_4)_2$ stoichiometric ratios implies that using a more THF-deficient $Mg(BH_4)_2{\cdot}x$THF adduct will reduce the amount of THF that might be released from the adduct during the concomitant thermal release of hydrogen. Indeed, thermal desorption measurements showed that such adducts with lower THF/$Mg(BH_4)_2$ ratios required higher temperatures to liberate THF. Hence, with respect to potential hydrogen-storage applications, the beneficial properties of the THF solvent can be retained over a greater temperature range while reducing the concentration of any unwanted impurity in the released hydrogen.

Conclusions

Various neutron scattering experiments, including NPD, NVS, FWS, and QENS, as well as molecular DFT calculations, were employed to gain deeper insights into the structural, vibrational, and dynamical properties of $Mg(BH_4)_2{\cdot}3THF$. Structural analysis has confirmed a lowering of the symmetry upon cooling, from monoclinic $C2/c$ to $P\bar{1}$ *via* a triclinic distortion, with the phase transition occurring around 200 K. Vibrational properties are strongly influenced by the THF environment. In particular, splitting in spectral features is observed and explained by the lowering of the overall symmetry. Interestingly, for the monoclinic structure, the orientational mobilities of the BH_4^- anions obtained from QENS are not particularly sensitive to the presence of THF and compare well with the mobilities of BH_4^- anions in unsolvated $Mg(BH_4)_2$. In contrast, a decrease in the BH_4^- jump frequencies is observed in the triclinic low-temperature structure and correlated with the enhanced steric effects presumably due to the smaller unit cell volume. Uniaxial jump reorientations of the BH_4^- anions around a two-fold (C_2, 180° jumps) axis are observed over the whole temperature range. The THF rings are also shown to be dynamically active, with orientational mobilities about an order of magnitude slower than for the BH_4^- anions, and with a reorientational mechanism also corresponding to uniaxial two-fold 180° jumps around the THF C_2 symmetry axis. In contrast, no noticeable reorientations of the THF rings are observed in the case of a more THF-deficient $2Mg(BH_4)_2{\cdot}THF$ adduct. This may be, at least in part, a consequence of a relatively stronger Mg^{2+}–THF bonding interaction, as the Mg^{2+} cation likely coordinates with only one THF molecule in this adduct. This is unlike THF-rich $Mg(BH_4)_2{\cdot}3THF$, where each Mg^{2+} cation coordinates with three THF molecules. Indeed, DFT calculations show a decrease in the binding energy with each additional THF coordinated to the Mg^{2+} cation.

Although the physicochemical behavior of this THF-solvated $Mg(BH_4)_2$ adduct determined from this combined experimental and computational study is of general fundamental interest, the observed and calculated interplay between Mg^{2+} cations, BH_4^- anions, and THF adduct molecules also has likely

 This journal is © the Owner Societies 2020

technological relevance toward understanding better the role of THF for improving the hydrogen desorption/absorption cycling properties of $Mg(BH_4)_2$. The dynamical results for different THF/$Mg(BH_4)_2$ stoichiometric ratios suggest little direct interaction, in general, between the THF molecules and the BH_4^- anions, whereas the THF–Mg^{2+} interaction is strongly ratio-dependent, with stronger interactions occurring for the lower THF/$Mg(BH_4)_2$ ratios. Hence, we would propose that using lower THF/$Mg(BH_4)_2$ ratios is beneficial to (i) preventing weakly bound THF from coming free from the Mg^{2+} cation and (ii) disrupting the stability of the crystalline phase leading to a lower melting point and enhanced kinetics.

Authors' contributions

M. D., T. A. and T. J. U. conceived and planned the experiments. M. D. and T. J. U. carried out the experiments. W. Z., I. N. and B. G. planned and carried out the DFT calculations. M. C. contributed to sample preparation. M. D., M. B., H. W., T. A., B. G., T. G., C. J. and T. J. U. contributed to the interpretation of the results. M. D. took the lead in writing the manuscript. All authors provided critical feedback and helped shape the research, analysis and manuscript.

Legal disclamer

The views and opinions of the authors expressed herein do not necessarily state or reflect those of the United States Government or any agency thereof. Neither the United States Government nor any agency thereof, nor any of their employees, makes any warranty, expressed or implied, or assumes any legal liability or responsibility for the accuracy, completeness, or usefulness of any information, apparatus, product, or process disclosed, or represents that its use would not infringe privately owned rights.

Conflicts of interest

The authors declare no competing financial interest.

Acknowledgements

M. D. gratefully acknowledges support from the US DOE Office of Energy Efficiency and Renewable Energy, Fuel Cell Technologies Office, under Contract No. DE-AC36-08GO28308. The authors gratefully acknowledge support from the Hydrogen Materials – Advanced Research Consortium (HyMARC), established as part of the Energy Materials Network under the U.S. Department of Energy, Office of Energy Efficiency and Renewable Energy, Fuel Cell Technologies Office. Pacific Northwest National Laboratory is a multi-program national laboratory operated by Battelle for the U.S. Department of Energy under Contract DE-AC05-76RL01830.

References

1 C. Liu, F. Li, L.-P. Ma and H.-M. Cheng, *Adv. Mater.*, 2010, **22**, E28–62.
2 N. P. Stadie, J. J. Vajo, R. W. Cumberland, A. A. Wilson, C. C. Ahn and B. Fultz, *Langmuir*, 2012, **28**, 10057–10063.
3 A. F. Gross, J. J. Vajo, S. L. Van Atta and G. L. Olson, *J. Phys. Chem. C*, 2008, **112**, 5651–5657.
4 D. Teichmann, W. Arlt, P. Wasserscheid and R. Freymann, *Energy Environ. Sci.*, 2011, **4**, 2767–2773.
5 N. L. Rosi, J. Eckert, M. Eddaoudi, D. T. Vodak, J. Kim, M. O'Keeffe and O. M. Yaghi, *Science*, 2003, **300**, 1127–1129.
6 S. Orimo, Y. Nakamori, J. R. Eliseo, A. Züttel and C. M. Jensen, *Chem. Rev.*, 2007, **107**, 4111–4132.
7 K. Chłopek, C. Frommen, A. Léon, O. Zabara and M. Fichtner, *J. Mater. Chem.*, 2007, **17**, 3496–3503.
8 Y. Nakamori, K. Miwa, A. Ninomiya, H. Li, N. Ohba, S. Towata, A. Züttel and S. Orimo, *Phys. Rev. B: Condens. Matter Mater. Phys.*, 2006, **74**, 045126.
9 N. Hanada, K. Chłopek, C. Frommen, W. Lohstroh and M. Fichtner, *J. Mater. Chem.*, 2008, **18**, 2611–2614.
10 G. L. Soloveichik, Y. Gao, J. Rijssenbeek, M. Andrus, S. Kniajanski, R. C. Bowman, S.-J. Hwang and J.-C. Zhao, *Int. J. Hydrogen Energy*, 2009, **34**, 916–928.
11 G. Severa, E. Rönnebro and C. M. Jensen, *Chem. Commun.*, 2010, **46**, 421–423.
12 H.-W. Li, K. Kikuchi, Y. Nakamori, K. Miwa, S. Towata and S. Orimo, *Scr. Mater.*, 2007, **57**, 679–682.
13 E. G. Bardají, N. Hanada, O. Zabara and M. Fichtner, *Int. J. Hydrogen Energy*, 2011, **36**, 12313–12318.
14 R. J. Newhouse, V. Stavila, S.-J. Hwang, L. E. Klebanoff and J. Z. Zhang, *J. Phys. Chem. C*, 2010, **114**, 5224–5232.
15 I. Saldan, C. Frommen, I. Llamas-Jansa, G. N. Kalantzopoulos, S. Hino, B. Arstad, R. H. Heyn, O. Zavorotynska, S. Deledda, M. H. Sørby, H. Fjellvåg and B. C. Hauback, Int. J. Hydrog, *Energy*, 2015, **40**, 12286–12293.
16 H. Hagemann, V. D'Anna, J.-P. Rapin, R. Černý, Y. Filinchuk, K. C. Kim, D. S. Sholl and S. F. Parker, *J. Alloys Compd.*, 2011, **509**(Suppl. 2), S688–S690.
17 E. G. Bardají, Z. Zhao-Karger, N. Boucharat, A. Nale, M. J. van Setten, W. Lohstroh, E. Röhm, M. Catti and M. Fichtner, *J. Phys. Chem. C*, 2011, **115**, 6095–6101.
18 A. Nale, M. Catti, E. G. Bardají and M. Fichtner, *Int. J. Hydrogen Energy*, 2011, **36**, 13676–13682.
19 J. Chen, Y. S. Chua, H. Wu, Z. Xiong, T. He, W. Zhou, X. Ju, M. Yang, G. Wu and P. Chen, *Int. J. Hydrogen Energy*, 2015, **40**, 412–419.
20 Y. Yang, Y. Liu, Y. Zhang, Y. Li, M. Gao and H. Pan, *J. Alloys Compd.*, 2014, **585**, 674–680.
21 S. Zhao, B. Xu, N. Sun, Z. Sun, Y. Zeng and L. Meng, *Int. J. Hydrogen Energy*, 2015, **40**, 8721–8731.
22 G. Soloveichik, J.-H. Her, P. W. Stephens, Y. Gao, J. Rijssenbeek, M. Andrus and J.-C. Zhao, *Inorg. Chem.*, 2008, **47**, 4290–4298.
23 M. Chong, T. Autrey, C. Jensen, M. Chong, T. Autrey and C. M. Jensen, *Inorganics*, 2017, **5**, 89.

Published on 20 November 2019. Downloaded on 12/31/2019 8:06:50 PM.

Published on 20 November 2019. Downloaded on 12/31/2019 8:06:50 PM.

24 The Mention of All Commercial Suppliers in This Paper Is for Clarity. This Does Not Imply the Recommendation or Endorsement of These Suppliers by NIST.
25 J. K. Stalick; E. Prince; A. Santoro; I. G. Schroder and J. J. Rush, Materials Science Applications of the New National Institute of Standards and Technology Powder Diffractometer, in *Neutron Scattering in Materials Science II*, ed. D. A. Neumann, T. P. Russell, B. J. Wuensch, Materials Research Society, Pittsburgh, 1995, vol. 376, pp. 101–106.
26 T. J. Udovic, C. M. Brown, J. B. Leão, P. C. Brand, R. D. Jiggetts, R. Zeitoun, T. A. Pierce, I. Peral, J. R. D. Copley, Q. Huang, D. A. Neumann and R. J. Fields, The Design of a Bismuth-Based Auxiliary Filter for the Removal of Spurious Background Scattering Associated with Filter-Analyzer Neutron Spectrometers, *Nucl. Instrum. Methods Phys. Res., Sect. A*, 2008, **588**, 406–413.
27 J. R. D. Copley and J. C. Cook, The Disk Chopper Spectrometer at NIST: A New Instrument for Quasielastic Neutron Scattering Studies, *Chem. Phys.*, 2003, **292**, 477–485.
28 A. Meyer, R. M. Dimeo, P. M. Gehring and D. A. Neumann, The High Flux Backscattering Spectrometer at the NIST Center for Neutron Research, *Rev. Sci. Instrum.*, 2003, **74**, 2759–2777.
29 R. T. Azuah, L. R. Kneller, Y. Qiu, P. L. W. Tregenna-Piggott, C. M. Brown, J. R. D. Copley and R. M. Dimeo, *J. Res. Natl. Inst. Stand. Technol.*, 2009, **114**, 341–358.
30 P. Giannozzi, S. Baroni, N. Bonini, M. Calandra, R. Car, C. Cavazzoni, D. Ceresoli, G. L. Chiarotti, M. Cococcioni, I. Dabo, A. D. Corso, S. de Gironcoli, S. Fabris, G. Fratesi, R. Gebauer, U. Gerstmann, C. Gougoussis, A. Kokalj, M. Lazzeri, L. Martin-Samos, N. Marzari, F. Mauri, R. Mazzarello, S. Paolini, A. Pasquarello, L. Paulatto, C. Sbraccia, S. Scandolo, G. Sclauzero, A. P. Seitsonen, A. Smogunov, P. Umari and R. M. Wentzcovitch, *J. Phys.: Condens. Matter*, 2009, **21**, 395502.
31 A. D. Becke, *J. Chem. Phys.*, 1993, **98**, 5648–5652.
32 C. Lee, W. Yang and R. G. Parr, *Phys. Rev. B: Condens. Matter Mater. Phys.*, 1988, **37**, 785–789.
33 S. H. Vosko, L. Wilk and M. Nusair, *Can. J. Phys.*, 1980, **58**, 1200–1211.
34 P. J. Stephens, F. J. Devlin, C. F. Chabalowski and M. J. Frisch, *J. Phys. Chem.*, 1994, **98**, 11623–11627.
35 G. A. Petersson, A. Bennett, T. G. Tensfeldt, M. A. Al-Laham, W. A. Shirley and J. Mantzaris, *J. Chem. Phys.*, 1988, **89**, 2193–2218.
36 G. A. Petersson and M. A. Al-Laham, *J. Chem. Phys.*, 1991, **94**, 6081–6090.
37 M. Valiev, E. J. Bylaska, N. Govind, K. Kowalski, T. P. Straatsma, H. J. J. Van Dam, D. Wang, J. Nieplocha, E. Apra, T. L. Windus and W. A. de Jong, *Comput. Phys. Commun.*, 2010, **181**, 1477–1489.
38 K. Momma and F. Izumi, *J. Appl. Crystallogr.*, 2011, **44**, 1272–1276.
39 M. Visseaux, M. Terrier, A. Mortreux and P. Roussel, *Eur. J. Inorg. Chem.*, 2010, 2867–2876.
40 E. B. Lobkovskii, L. V. Titov, S. B. Psikha, M. Y. Antipin and Y. T. Struchkov, *J. Struct. Chem.*, 1983, **23**, 644–646.
41 Y. Filinchuk, R. Černý and H. Hagemann, *Chem. Mater.*, 2009, **21**, 925–933.
42 M. Dimitrievska, J. L. White, W. Zhou, V. Stavila, L. E. Klebanoff and T. J. Udovic, *Phys. Chem. Chem. Phys.*, 2016, **18**, 25546–25552.
43 B. Cadioli, E. Gallinella, C. Coulombeau, H. Jobic and G. Berthier, *J. Phys. Chem.*, 1993, **97**, 7844–7856.
44 M. I. Aroyo, J. M. Perez-Mato, C. Capillas, E. Kroumova, S. Ivantchev, G. Madariaga, A. Kirov and H. Wondratschek, *Z. Kristallogr. – Cryst. Mater.*, 2009, **221**, 15–27.
45 M. I. Aroyo, A. Kirov, C. Capillas, J. M. Perez-Mato and H. Wondratschek, *Acta Crystallogr., Sect. A: Found. Crystallogr.*, 2006, **62**, 115–128.
46 M. Bee, *Quasielastic Neutron Scattering, Principles and Applications in Solid State Chemistry, Biology and Materials Science*, CRC Press, Bristol, England, Philadelphia, 1988.
47 D. Blanchard, J. B. Maronsson, M. D. Riktor, J. Kheres, D. Sveinbjörnsson, E. Gil Bardají, A. Léon, F. Juranyi, J. Wuttke, K. Lefmann, B. C. Hauback, M. Fichtner and T. Vegge, *J. Phys. Chem. C*, 2012, **116**, 2013–2023.
48 A. V. Skripov, A. V. Soloninin, O. A. Babanova, H. Hagemann and Y. Filinchuk, *J. Phys. Chem. C*, 2010, **114**, 12370–12374.

 This journal is © the Owner Societies 2020

Electronic Supplementary Material (ESI) for Physical Chemistry Chemical Physics.
This journal is © the Owner Societies 2019

Supporting Information for:

Structural and Reorientational Dynamics of Tetrahydroborate (BH_4^-) and Tetrahydrofuran (THF) in $Mg(BH_4)_2 \cdot 3THF$ Adduct: Neutron-Scattering Characterization

Mirjana Dimitrievska,*[,1,2] Marina Chong,[3] Mark E. Bowden,[3] Hui Wu,[2] Wei Zhou,[2] Iffat Nayyar,[3] Bojana Ginovska,[3] Thomas Gennett,[1] Tom Autrey,[3] Craig M. Jensen,[4] and Terrence J. Udovic[2]

[1]National Renewable Energy Laboratory (NREL), 5013 Denver W Pkwy, Golden, CO 80401, United States

[2]NIST Center for Neutron Research, National Institute of Standards and Technology, Gaithersburg, MD 20899-6102, United States

[3]Pacific Northwest National Laboratory (PNNL), Richland, WA 99352, United States

[4]University of Hawaii Manoa, Department of Chemistry, Honolulu, HI 96822-2275, United States

*Author to whom correspondence should be addressed. E-mail: mirjana.dimitrievska@nist.gov; mirjana.dimitrievska@nrel.gov;

N.B., for all the following figures, standard uncertainties are commensurate with the observed scatter in the data, if not explicitly designated by vertical error bars.

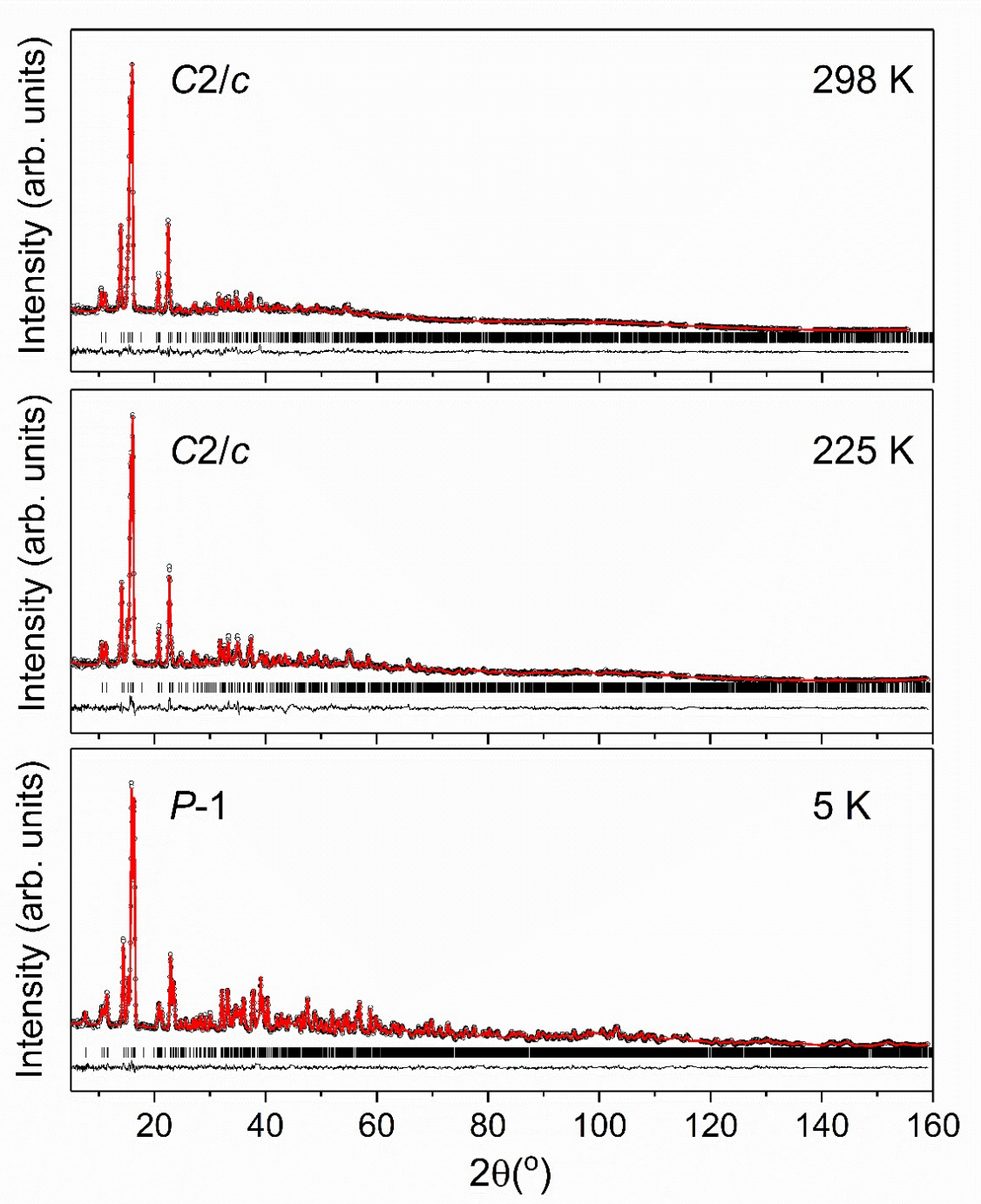

Figure S1. Temperature-dependent NPD patterns [λ = 1.5397 Å] and model refinements for $Mg(BH_4)_2 \cdot 3TDF$ at 5 K (*P*-1), 225 K (*C*2/*c*), and 298 K (*C*2/*c*): experimental data (black circles), fitted patterns (red lines), and differences (black lines beneath the patterns). Vertical bars indicate the calculated positions of Bragg peaks. Extra peaks from Al container are excluded.

Table S1. The refined $Mg(BH_4)_2 \cdot 3TDF$ structural parameters derived from the NPD data.

***T* (K)**	**5**	**225**	**298**
Symmetry	*P*-1	*C*2/*c*	*C*2/*c*
***a* (Å)**	8.3616(4)Å	11.960(1)	12.115(2)
***b* (Å)**	8.6328(4)	12.490(1)	12.623(2)
***c* (Å)**	12.2557(5)	19.949(2)	20.199(4)
α (°)	102.5965(33)	90	90
β (°)	103.984(4)	144.456(3)	144.992(4)
γ (°)	92.2394(32)	90	90
***V* (Å^3)**	833.84(6)	1732.5(2)	1772.2(2)
Z	8	4	4
R_{wp}	0.0172	0.0191	0.0157
R_p	0.0144	0.0166	0.0136
χ^2	1.43	1.22	1.21

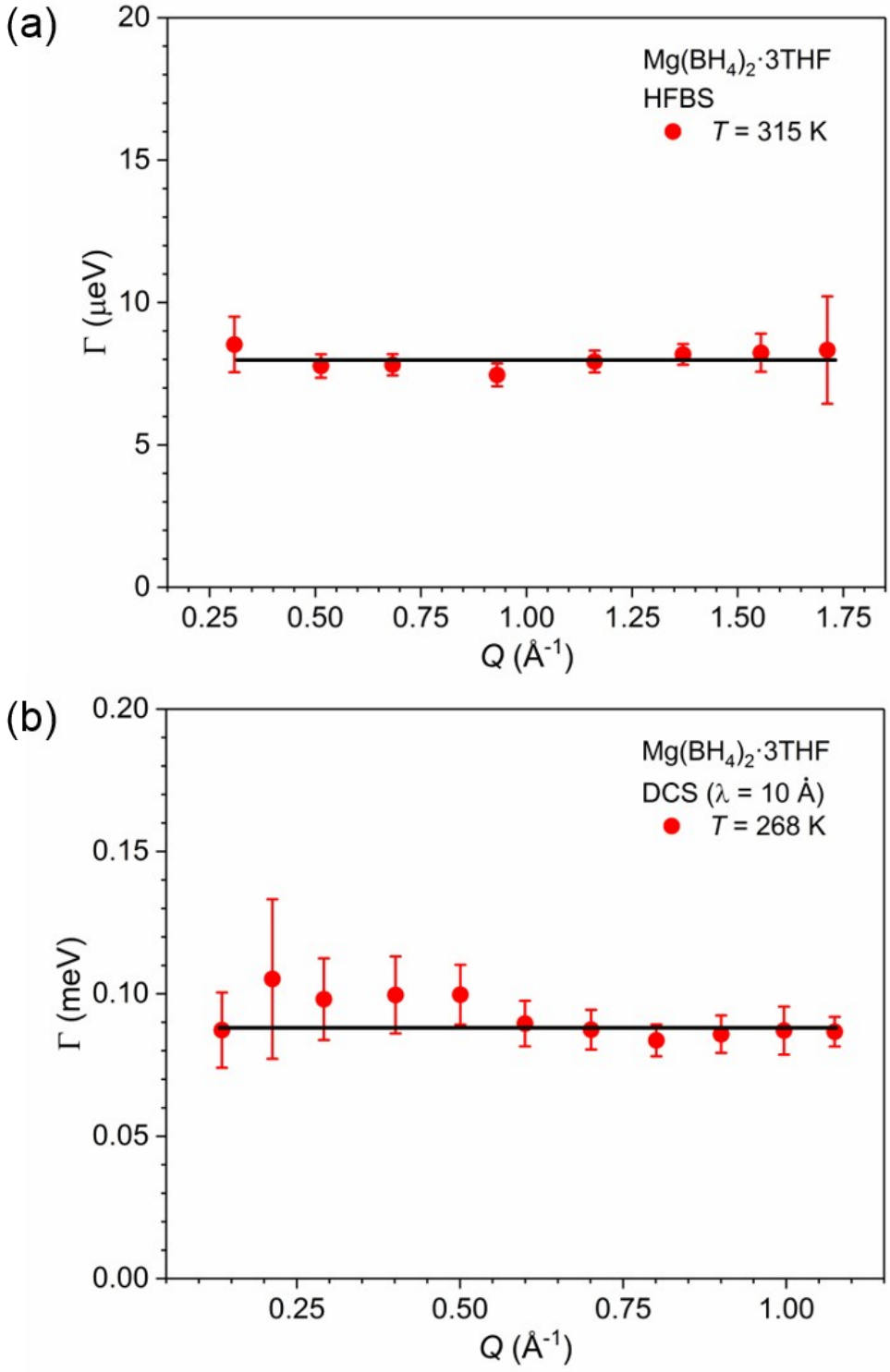

Figure S2. *Q*-dependence of the Lorentzian (quasielastic) fwhm linewidths for $Mg(BH_4)_2 \cdot 3THF$ obtained on (a) the HFBS spectrometer at 315 K, and (b) the DCS spectrometer at 268 K.

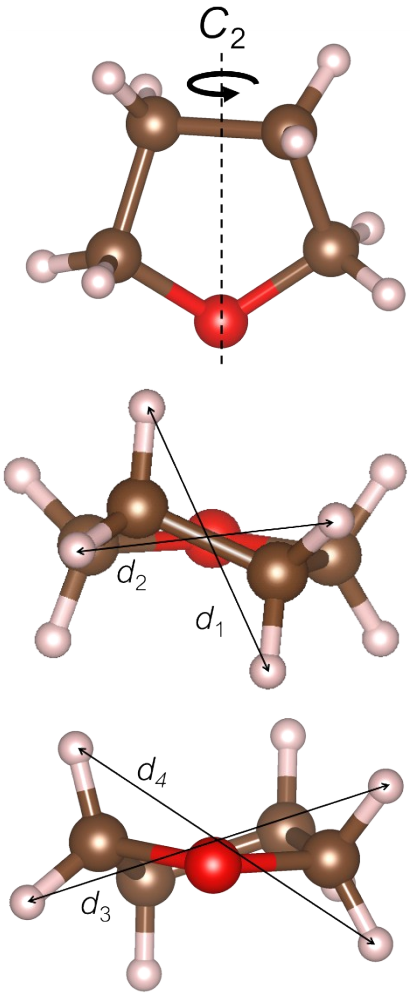

Figure S3. Three views of THF groups. Red, brown and pink spheres denote the respective O, C and H atoms. Distances used in this study to represent the "ideal" anion polyhedral size and shape are estimated from the room-temperature neutron powder diffraction results for $Mg(BH_4)\cdot 3TDF$.

Table S2. Binding energies for THF in (kJ/mol) [E – total energy, E_{zpc} – binding energy, H – enthalpy; G – free Gibss energy]

Reaction	E	E_{zpc}	H	G
$Mg(BH_4)_2$+THF → $Mg(BH_4)_2$·THF	-91.9	-85.7	-85.0	-37.8
$Mg(BH_4)_2$·THF+THF→$Mg(BH_4)_2$·2THF	-66.4	-60.7	-59.9	-11.1
$Mg(BH_4)_2$·2THF+THF→$Mg(BH_4)_2$·3THF	-29.0	-23.0	-22.4	30.0

Table S3. Absolute energies for the molecular structures (in hartree) [E – total energy, E_{zpc} – binding energy, H – enthalpy; G – free Gibss energy]

Structure	E	E_{zpc}	H	G
$Mg(BH_4)_2$	-254.6226	-254.54428	-254.53674	-254.57294
THF	-232.45938	-232.34218	-232.33631	-232.37094
$Mg(BH_4)_2$·THF	-487.11710	-486.91914	-486.90544	-486.95830
$Mg(BH_4)_2$·2THF	-719.60180	-719.28445	-719.26458	-719.33347
$Mg(BH_4)_2$·3THF	-952.07226	-951.63541	-951.60944	-951.69296

Table S4. Optimized structures in angstroms (Å)

DFT (B3LYP/6-31+G)

$Mg(BH_4)_2$			
Mg	0.27155728	0.00110728	-0.00169945
B	0.35334054	2.10157160	-0.01075611
B	0.18690129	-2.09898265	0.00703603
H	0.70888078	-1.66581838	-1.04006706
H	0.14003901	-3.29012383	0.01258057
H	0.85807208	-1.66303174	0.96411819
H	-0.95090907	-1.59462912	0.09094832
H	0.39983746	3.29275831	-0.01568733
H	-0.31701871	1.66519965	-0.96769047
H	-0.16739333	1.66708403	1.03650077
H	1.49194314	1.59900711	-0.09487669
THF			
O	0.01523478	-1.16914638	-0.41043542
C	1.14466242	-0.45125379	0.08462154
H	1.32481825	-0.72314192	1.13836297
H	2.01287221	-0.75273836	-0.50730549
C	-1.13002443	-0.46407659	0.06634880
H	-1.98515459	-0.77528297	-0.53942375
H	-1.32399506	-0.73806967	1.11708761
C	0.77759474	1.04271712	-0.04460302
H	1.17074435	1.45898011	-0.97762970
H	1.18845673	1.63364650	0.78084353
C	-0.77779314	1.03394602	-0.05710065
H	-1.20851141	1.62013191	0.76157907
H	-1.16057046	1.44584944	-0.99635537
$Mg(BH_4)_2 \cdot THF$			
Mg	-0.14285001	1.75585963	-0.03458671
O	0.00856405	-0.30358883	-0.01864692
B	-2.23334503	2.28261937	0.12827051
B	1.84837632	2.57998165	-0.20783754
H	1.05207765	3.51666348	-0.19860699
H	2.98562663	2.94180865	-0.29762941
H	1.67941298	1.92580939	0.84152826
H	1.54925980	1.83425431	-1.16114602
H	-3.41133814	2.47579689	0.21373813
H	-1.96942817	1.64418724	-0.91113806
H	-1.82950543	1.60329775	1.09254405
H	-1.58234651	3.32532593	0.10370471

C	1.25266841	-1.05214492	-0.21756652
C	-1.11272027	-1.22304940	0.19331815
C	-0.56996811	-2.59714779	-0.19015226
H	-1.39412095	-1.16635554	1.25006340
H	-1.94639191	-0.87459581	-0.41847353
C	0.91644452	-2.48481155	0.18765625
H	1.52399100	-0.97115736	-1.27536093
H	2.02556483	-0.57595533	0.38789960
H	1.05074330	-2.62145238	1.26726581
H	1.54817356	-3.21388548	-0.32860642
H	-1.08866090	-3.40272130	0.33821194
H	-0.68161164	-2.76872125	-1.26734540
$Mg(BH_4)_2 \cdot 2THF$			
Mg	1.03381577	-0.20407512	-0.40488750
O	0.01333143	1.55708858	0.16605102
O	-0.40920979	-1.70166410	-0.02442706
C	-0.38846034	-2.58772739	1.13705373
C	-0.96837767	-3.90657552	0.63579560
C	-1.99565920	-3.43524767	-0.40556244
C	-1.28642838	-2.24936727	-1.05990864
B	1.13163557	-0.08583528	-2.62211695
B	2.57023759	-0.49458468	1.17682641
H	2.53268781	-1.45688008	0.40241670
H	3.41161590	-0.65017825	2.01960079
H	2.79158726	0.52250361	0.51036544
H	1.45064048	-0.37604760	1.68882497
H	1.55024882	-1.17116694	-2.20447120
H	-0.03667290	0.04114991	-2.23651941
H	1.19134307	-0.03267808	-3.82044691
H	1.80108884	0.81054901	-2.09834197
H	-1.41241269	-4.49527190	1.44460100
H	-0.18647473	-4.51124235	0.16132964
H	0.64162300	-2.64721862	1.48868716
H	-1.01164576	-2.13417998	1.91752426
H	-0.65789547	-2.54669454	-1.90410865
H	-1.95961199	-1.45254849	-1.38411160
H	-2.25597739	-4.20725825	-1.13619543
H	-2.91943748	-3.11041999	0.08870347
C	0.25475339	2.27960013	1.41288081
C	-0.69870789	2.41389825	-0.78275157
C	-1.09201757	3.65958887	0.01155553
H	-0.01494723	2.63682775	-1.60669979
H	-1.54844694	1.84829033	-1.17172888
C	0.02001737	3.74706423	1.06868042
H	-0.46049013	1.91189637	2.15873549

H	1.26773614	2.04473213	1.73994768
H	0.92744421	4.18806960	0.63948656
H	-0.26398798	4.33579617	1.94653285
H	-1.15284281	4.54672392	-0.62630956
H	-2.06748342	3.52048008	0.49351939
$Mg(BH_4)_2 \cdot 3THF$			
C	1.65712819	2.86039468	-0.77980693
O	0.49750713	2.13579059	-0.25889606
C	-0.28082575	3.00376730	0.61355087
C	0.55476148	4.27152452	0.79117133
C	1.34813276	4.33212321	-0.52393206
Mg	0.62322062	0.00798601	-0.00688577
O	-1.53213778	-0.03564749	0.00650197
O	0.57263130	-2.13953908	0.28986438
C	1.44858693	-2.87215328	1.18524164
C	2.27965719	-3.75120505	0.25132264
C	1.30093416	-4.08016599	-0.90686906
C	0.12960094	-3.09452546	-0.70732217
B	1.48736685	-0.29085081	-2.28246716
B	1.53274933	0.43664622	2.23015345
H	2.21656717	0.20973057	1.21554202
H	1.88291286	-0.32863223	3.10208015
H	1.65240383	1.60771240	2.52558060
H	0.33292574	0.20742671	1.98672269
H	1.75692674	-1.39416629	-2.70984177
H	0.28169601	-0.27779995	-1.97349343
H	1.67610838	0.60686012	-3.07500142
H	2.18223469	-0.07995574	-1.27332294
H	1.23376322	4.15459703	1.64280269
H	-0.06886298	5.15491148	0.96317281
H	-1.23377053	3.21057215	0.10948725
H	-0.46287541	2.47059838	1.54812649
H	1.76291586	2.58398643	-1.82902830
H	2.53977932	2.52678847	-0.22295787
H	0.73130551	4.74448616	-1.33231470
H	2.25886067	4.93464863	-0.44864553
H	2.65424280	-4.64623926	0.75855016
H	3.13891613	-3.18663919	-0.12306292
H	2.00815645	-2.14168800	1.76727090
H	0.82099326	-3.47038013	1.86196793
H	-0.12498005	-2.53129784	-1.60395537
H	-0.76422227	-3.60026925	-0.31543768
H	1.77586083	-3.92728458	-1.87920623
H	0.94669602	-5.11540933	-0.85993313
C	-2.32687409	-0.64548567	1.06544734

C	-2.39165805	0.40535779	-1.08339702
C	-3.73568020	-0.27417299	-0.82999807
H	-2.47060119	1.49803421	-1.03487621
H	-1.90821076	0.12616082	-2.02130934
C	-3.78151771	-0.34154927	0.70544717
H	-2.11524511	-1.72033619	1.06628158
H	-1.99912706	-0.22068609	2.01672229
H	-4.08809603	0.62542005	1.12225247
H	-4.46689643	-1.10580210	1.08489505
H	-4.56970948	0.28667574	-1.26321830
H	-3.74371323	-1.28273206	-1.26066895

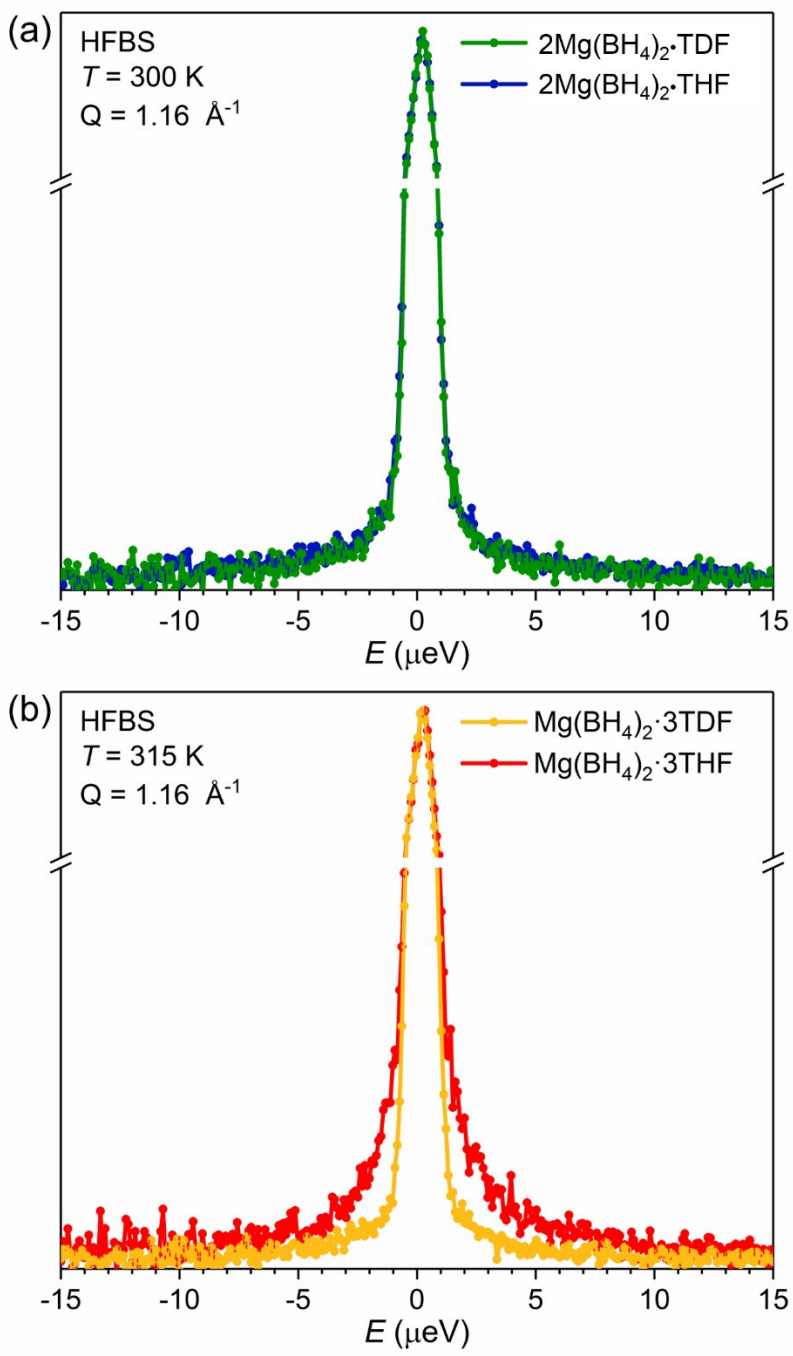

Figure S4. Comparison of QENS spectra for (a) $2Mg(BH_4)_2 \cdot TDF$ and $2Mg(BH_4)_2 \cdot THF$ at 300K, and (b) $Mg(BH_4)_2 \cdot 3TDF$ and $Mg(BH_4)_2 \cdot 3THF$ measured at 315 K on HFBS at Q = 1.16 Å^{-1}, 0.8 μeV resolution. No additional broadening is observed between the QENS spectra of $2Mg(BH_4)_2 \cdot TDF$ and $2Mg(BH_4)_2 \cdot THF$, leading to the conclusion that the THF dynamics in this case is much slower than the detection limit of the instrument. In contrast, considerable differences in the QENS spectra of $Mg(BH_4)_2 \cdot 3TDF$ and $Mg(BH_4)_2 \cdot 3THF$ showing that the THF rings are orientationally mobile.

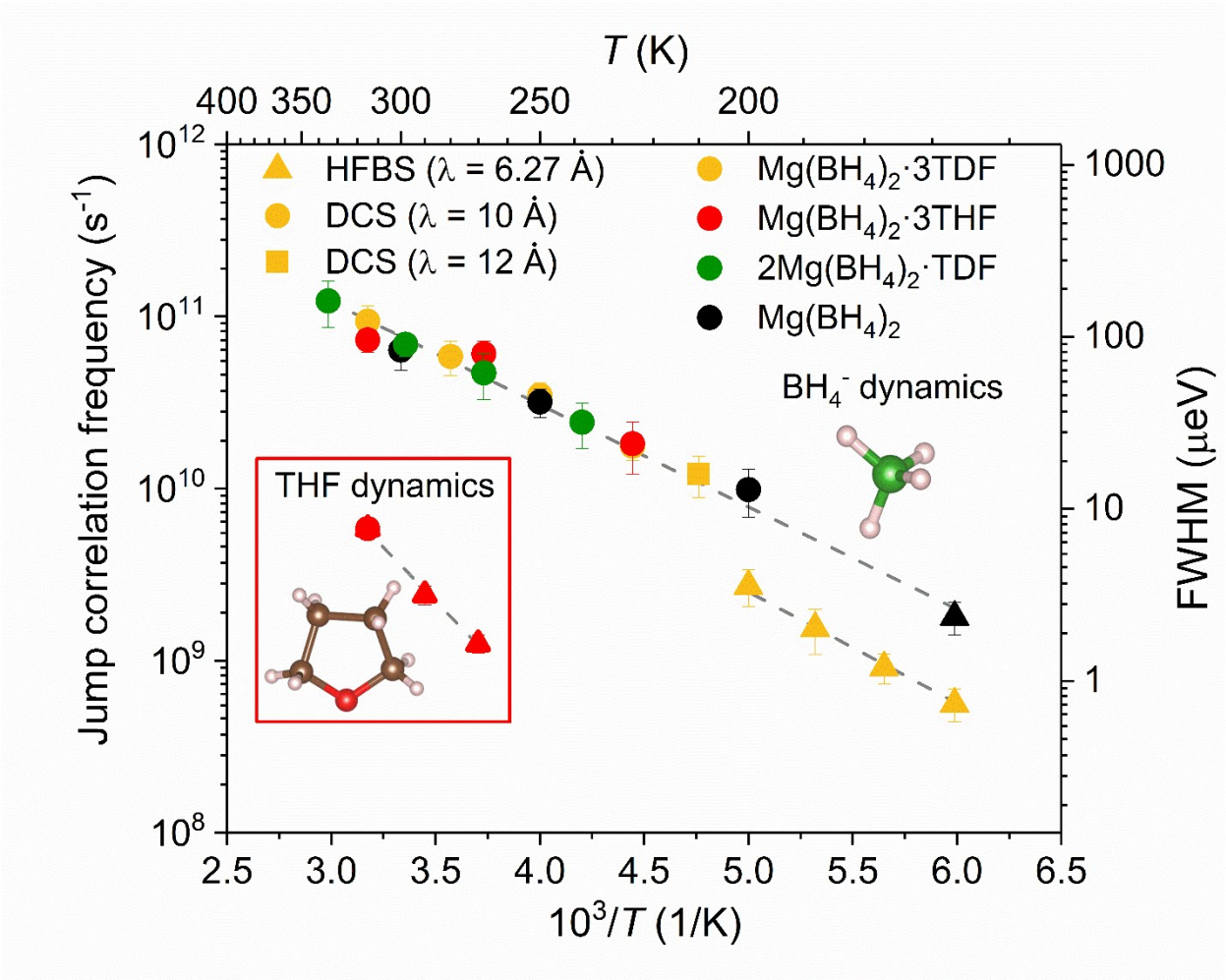

Figure S5. Jump correlation frequencies τ_{i1}^{-1} vs. inverse temperature for $Mg(BH_4)_2 \cdot 3TDF$, $Mg(BH_4)_2 \cdot 3THF$, $2Mg(BH_4)_2 \cdot TDF$ and pristine $Mg(BH_4)_2$. Different symbols denote the different instruments used. Different colors denote the different samples. Dashed lines represent linear fits to the QENS data.

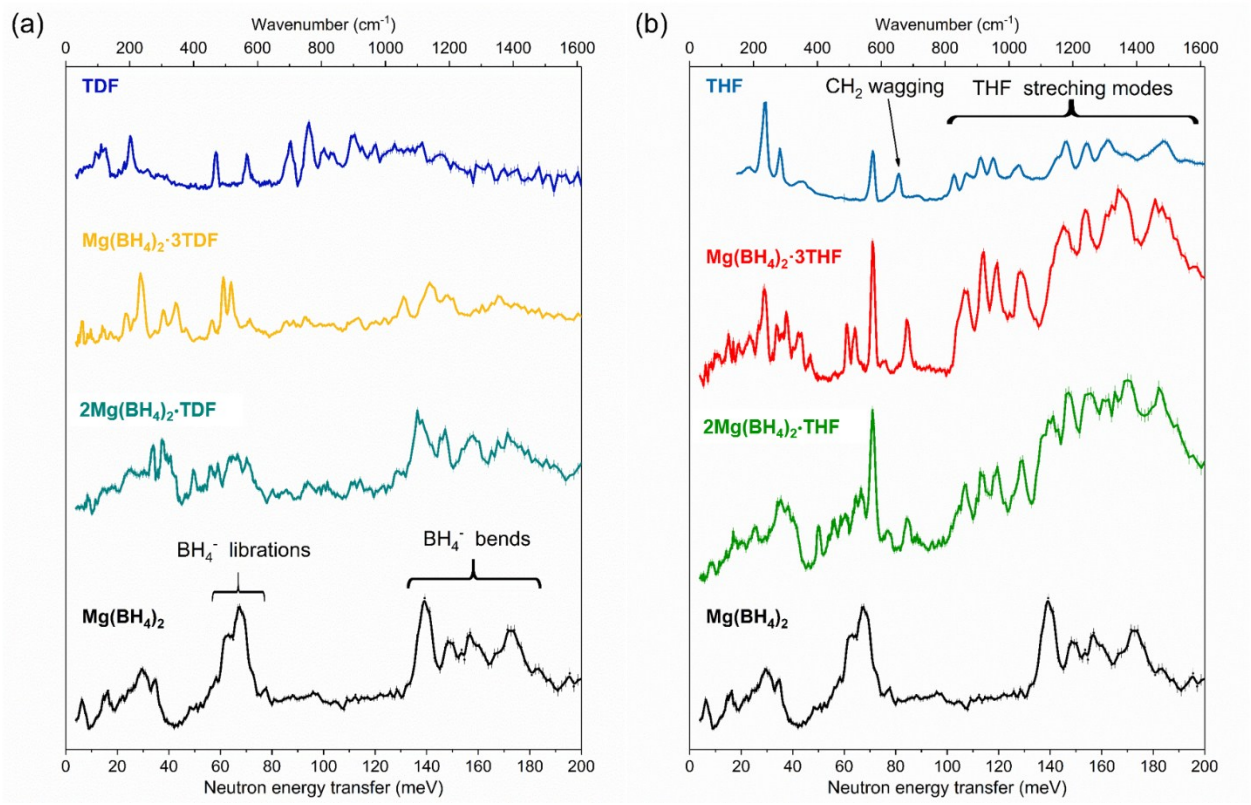

Figure S6. Comparison of the NVS spectra for (a) $Mg(BH_4)_2$, $2Mg(BH_4)_2{\cdot}TDF$, $Mg(BH_4)_2{\cdot}3TDF$ and TDF, and (b) $Mg(BH_4)_2$, $2Mg(BH_4)_2{\cdot}THF$, $Mg(BH_4)_2{\cdot}3THF$ and THF measured at 4K. The Cu(220) and pyrolytic graphite (002) monochromators were used above and below 40 meV, respectively. Vertical error bars denote ±1 σ. A slight decrease in the frequency of the BH_4^- librational and bending modes is observed with the increase in THF content. This can be explained by the changes in the intramolecular interactions. The red shift of the BH_4^- modes reflects the elongation in the Mg-B bond length caused by a changed Mg^{2+}-THF coordination, as confirmed by the DFT calculations.

Elastic Incoherent Structure Factor (EISF) calculation for the THF molecule

For the reorientational dynamics of the THF molecule and BH_4^- anions situated within a solid lattice of $Mg(BH_4)_2 \cdot 3THF$, the EISF for each due to the H-atom reorientions can be written as:

$$EISF(THF) = \frac{E_{THF}}{E_{THF} + q_{THF}} \tag{S1}$$

$$EISF(BH_4^-) = \frac{E_{BH_4^-}}{E_{BH_4^-} + q_{BH_4^-}} \tag{S2}$$

where E_{THF} and q_{THF} are the respective elastic and quasielastic scattering intensity contributions due only to the THF reorientational dynamics, while $E_{BH_4^-}$ and $q_{BH_4^-}$ are the respective elastic and quasielastic scattering intensity contributions due only to the BH_4^- reorientational dynamics. Similarly, the EISF [EISF(total)] of the $Mg(BH_4)_2 \cdot 3THF$ adduct can be calculated as the total elastic scattering intensity coming from both THF molecules and BH_4^- anions, divided by the sum of their total elastic and quasielastic scattering intensity contributions:

$$EISF(total) = \frac{E_{THF} + E_{BH_4^-}}{E_{THF} + E_{BH_4^-} + q_{THF} + q_{BH_4^-}} \tag{S3}$$

On the other hand, the EISF(total) can also be calculated as a weighted sum of the partial EISFs of the THF^- molecule and BH_4^- anions by including the appropriate weighting factors based on the number of H atoms associated with each chemical group. Considering that there are a total of 32 H atoms with 24 present in the three THF rings and 8 present in the two BH_4^- anions, the total EISF is given as:

$$EISF(total) = \frac{24}{32} \cdot EISF(THF) + \frac{8}{32} \cdot EISF\left(BH_4^-\right) \tag{S4}$$

Finally, substituting Eq. (S1), (S2) and (S3) in the Eq. (S4), the following equation is obtained:

$$\frac{E_{THF} + E_{BH_4^-}}{E_{THF} + E_{BH_4^-} + q_{THF} + q_{BH_4^-}} = \frac{24}{32} \cdot \frac{E_{THF}}{E_{THF} + q_{THF}} + \frac{8}{32} \cdot \frac{E_{BH_4^-}}{E_{BH_4^-} + q_{BH_4^-}} \tag{S5}$$

In the HFBS data measured, the elastic scattering intensity contribution is actually the sum of the elastic peak intensities due to both THF and BH_4^- reorientations:

$$E_T = E_{THF} + E_{BH_4^-} \tag{S6}$$

whereas the fitted quasielastic scattering intensity contribution is due only to the slower THF reorientations (q_{THF}). Both values, (E_T and q_{THF}) can be obtained directly from the fits of the QENS data measured on the HFBS instrument. The much faster BH_4^- reorientations yield quasielastic scattering ($q_{BH_4^-}$) that is an order of magnitude too broad to be observed by HFBS and resides as broad background scattering buried under the flat baseline and cannot be directly determined from the HFBS measurements.

In order to extract the EISF solely due to the THF molecules, it is necessary to determine the amount of THF elastic scattering intensity (E_{THF}), as the quasielastic contribution (q_{THF}) is already known directly from the fits of the QENS measurements. This can be done with the aid of Eq. (S5) and (S6), and the fact that the EISF behavior for the BH_4^- anions is known, and can be calculated as:

$$EISF\left(BH_4^-\right) = \frac{1}{2}\left(1 + j_0(Qd)\right) = \frac{E_{BH_4^-}}{E_{BH_4^-} + q_{BH_4^-}} \tag{S7}$$

where $j_0(x)$ is a zeroth-order Bessel function equal to $\sin(x)/(x)$, and $d \approx 2.0$ Å is the jump distance between two BH_4^- hydrogen atom positions.

Considering Eq. (S5), (S6) and (S7), as well as the known variables (E_T, q_{THF}, and $EISF\left(BH_4^-\right)$), it is possible to calculate the THF elastic scattering intensity (E_{THF}) as:

$$E_{THF} = \frac{3 \cdot E_T - EISF\left(BH_4^-\right) \cdot q_{THF}}{3 + EISF\left(BH_4^-\right)} \tag{S8}$$

The EISF solely due to the THF molecules can then be calculated by inserting Eq. (S8) into the Eq. (S1):

$$EISF(THF) = \frac{3 \cdot E_T - EISF\left(BH_4^-\right) \cdot q_{THF}}{3 \cdot \left(E_T + q_{THF}\right)} \tag{S9}$$

How to view phonon animations using the V_Sim software*

The animation files named as **file_name_anime.ascii**, contain the information needed to view the animated (gamma-point) phonon normal modes from the DFT-optimized structures, respectively, and can be opened following the steps below:

- Get the V_Sim software (It is free, and there is no need to install).
- Go to the following webpage and download the Win32 binaries:
  http://inac.cea.fr/L_Sim/V_Sim/download.html
- Unzip the zip file to wherever you want to put the software.
- Click "~V_Sim\bin\V_sim.exe" to start the V_Sim program, then open the **file_name_anime.asci** file to view the phonon animations.
- To build bonds in the structure, check the box on the left side of the "Pairs" button, and click the "Pairs" button.
- Highlight a pair and click the "Auto set" button to allow bonding.
- Adjust the "Link parameters," if desired.
- Adjust the element color, radius, etc. on the "Elements" tab, if desired.
- Go to the "Phonons" tab, highlight a phonon mode, and click the "Play" button to view a phonon animation. N.B. The mode energies are indicated in wavenumbers cm^{-1} (1 meV ≈ 8.066 cm^{-1}).

* N.B., the use of this software does not imply its recommendation or endorsement by NIST